JGR Solid Earth

RESEARCH ARTICLE
10.1029/2022JB024750

Excitation of Back-Arc Tsunamis From Megathrust Ruptures: Theory and Application to the Sea of Japan

Amir Salaree[1] **and Yihe Huang**[1]

[1]Department of Earth and Environmental Sciences, University of Michigan, Ann Arbor, MI, USA

Key Points:

- We present theoretical and numerical models of back-arc tsunamis produced by megathrust earthquakes
- Among source parameters, seismic moment and fault dip angles determine the dominant period and the spread of back-arc tsunamis
- Back-arc tsunamis from Japan Trench rupture scenarios can reach amplitudes >1 m in the Sea of Japan, and should be included in hazard models

Supporting Information:

Supporting Information may be found in the online version of this article.

Correspondence to:

A. Salaree,
salaree@umich.edu

Citation:

Salaree, A., & Huang, Y. (2023). Excitation of back-arc tsunamis from megathrust ruptures: Theory and application to the Sea of Japan. *Journal of Geophysical Research: Solid Earth*, *128*, e2022JB024750. https://doi.org/10.1029/2022JB024750

Received 17 MAY 2022
Accepted 14 JAN 2023

Author Contributions:

Conceptualization: Amir Salaree
Data curation: Amir Salaree
Formal analysis: Amir Salaree
Funding acquisition: Yihe Huang
Investigation: Amir Salaree, Yihe Huang
Methodology: Amir Salaree
Project Administration: Yihe Huang
Resources: Yihe Huang
Software: Amir Salaree
Supervision: Yihe Huang
Validation: Amir Salaree, Yihe Huang
Visualization: Amir Salaree
Writing – original draft: Amir Salaree
Writing – review & editing: Amir Salaree, Yihe Huang

Abstract Large megathrust ruptures can create notable tsunamis in tectonic back-arc basins as was documented during the 2011 Tohoku earthquake in the Sea of Japan. We present a physical analysis of the excitation of back-arc tsunamis by extending the fore-arc deformation field from the earthquake centroid into the back-arc basin and identify fault dip as the main geometrical contributor to the propagation of these events. As such, our theoretical model along with a large number of numerical simulations reveal that the dominant period of back-arc tsunamis is different from that of the fore-arc waves and thus they are a new class of tsunamis. Through numerical simulations and analysis of data from the 2011 Tohoku event, we show that a combination of near- to intermediate-field horizontal and vertical deformation as well as transient surface waves is necessary to reconstruct the back-arc propagation. We find that while seismic surface waves can affect coastal tsunami amplitudes in the back-arc, their effect comes second to that of the horizontal component of deformation as manifested via bathymetric gradient. We then simulate back-arc tsunamis and the hazard in the Sea of Japan from several potential future earthquake scenarios in the Japan Trench and Nankai Trough. Our results show that the coseismic excitation of back-arc tsunamis can result in considerable waves close to 1 m in the Sea of Japan, near the Niigata Prefecture from megathrust earthquakes.

Plain Language Summary The 2011 Japan earthquake created a large tsunami in the Pacific Ocean. But it also made a moderate tsunami in the Sea of Japan, on the far side of the Japanese islands. We call these waves Back-arc tsunamis and study their properties by looking at the contributions of various earthquake aspects including earthquake size, depth, fault geometry, and seismic surface waves, to the generation of these tsunamis. Our work shows that contrary to regular tsunamis, the hazard from back-arc tsunamis is affected by the fault dip angle (how steep the fault is). We also find that large earthquakes in eastern Japan can create relatively large back-arc tsunamis (with wave heights exceeding 1 m) in the Sea of Japan.

1. Background and Motivation

Large megathrust earthquakes are often associated with tsunamis near the main deformation fronts at the fore-arc, for example, 2004 Sumatra (e.g., Lay et al., 2005) and 2011 Tohoku (e.g., Mori et al., 2011). However, secondary tsunamis have been reported in the tectonic back-arc basins during these same events by Grue et al. (2008) and Murotani et al. (2015). In the case of the 2011 Japan event, the so-called back-arc tsunami was reported to reach an amplitude of ~50 cm and recorded by tide gauges around the Sea of Japan. Moderate waves were also reported by local fishermen at Niigata Prefecture (Murotani, *personal. comm.*).

The coseismic excitation of back-arc tsunamis is inherently different from the leakage of tsunamis into such basins from outside sources through narrow opening. The latter mechanism has been previously modeled by Shevchenko et al. (2014) for the passage of the 2011 Tohoku tsunami into the Sea of Japan and the Sea of Okhotsk through the Tsugaru and Yuzhno-Kurilsk Straits, respectively (Figure 1). However, this mechanism cannot explain the fact that the back-arc tsunami arrivals at the tide gauges in the Sea of Japan matched the origin time of coseismic rupture, not those of the fore-arc waves arriving much later. Murotani et al. (2015) have instead concluded that such tsunami waves were excited coseismically and modeled the tsunami (perhaps the best documented event of this kind so far) using both vertical and horizontal components based on Okada's (1985) algorithm. In other studies of the complexity of the 2011 tsunami waveforms in Korea, Lee et al. (2016) and Kim et al. (2019) attributed the mismatch between synthetic and observed waveforms to the tsunami arriving from the north, that is, the Sea of Japan (Figure 1), concluding that the coseismic rupture of the Tohoku event excited the back-arc tsunami. We note that in Figure 1, while generally it is expected that $T_3 > T_2 > T_1$, beaming the simulated tsunami shows that the first and second rays have similar travel times ($T_1 \approx T_2$) as also documented by Kim et al. (2019).

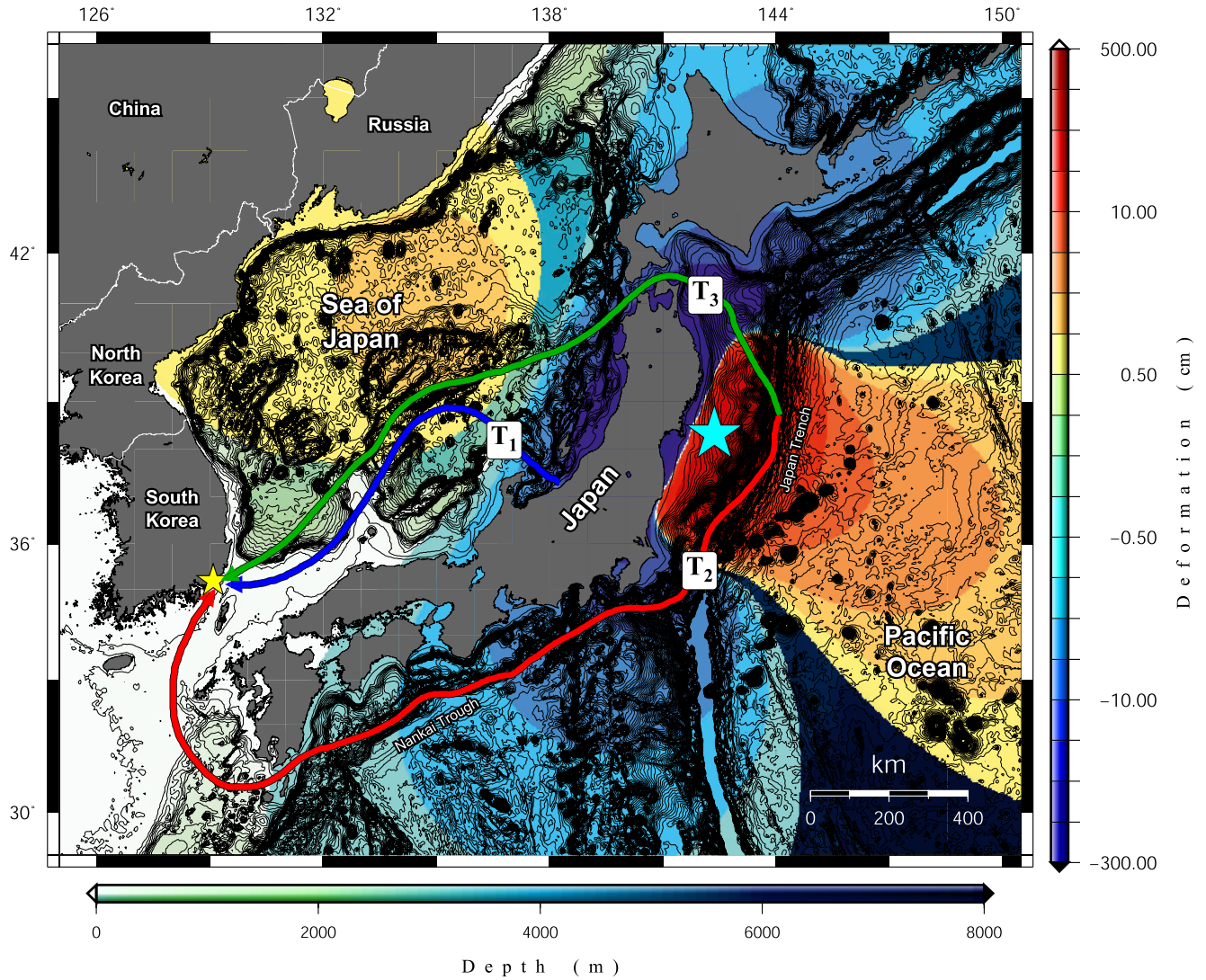

Figure 1. The three different approximate paths and their corresponding arrival times (T_i) for the 2011 tsunami to have reached Busan, Korea (yellow star) in the back-arc Sea of Japan. The colored background shows the offshore static, coseismic deformation field calculated from the CMT solution (Dziewonski et al., 1981; Ekström et al., 2012) of the mainshock. Black contours represent bathymetry (GEBCO, 2021). Fault dimensions are calculated using earthquake scaling laws (Geller, 1976).

Nevertheless, the listed previous studies do not investigate the contribution of various source and basin factors to the frequency content of the back-arc tsunamis. While Murotani et al. (2015) reported the poor mismatch in the high-frequency tsunami arrivals earlier in the waveform, Kim et al. (2019) applied a band-pass filter of 5 min–6 hr to the tsunami waveforms and did not consider the high-frequency tsunami arrivals in their analysis. As a result, the behavior of back-arc tsunamis and their hazard at both high and low frequencies remain ambiguous.

The energy and hence the dominant period of fore-arc tsunamis is generally controlled by the ratio of water depth to source size (Okal, 2021), which for large earthquakes is traditionally considered proportional to the displaced volume of water, that is, the hydrodynamic length scale of earthquake rupture (e.g., Plafker, 1997; Rabinovich, 1997; Okal & Synolakis, 2004). Note that length scale is a dimension in hydrodynamic problems used to provide an expected order of magnitude for hydrodynamic velocity or dislocation features (Kundu et al., 2015). The hazard associated with fore-arc tsunamis in the near-field is mainly a function of source geometry and dimensions (e.g., Okal & Synolakis, 2004; Satake et al., 2022) as well as coastal morphology (e.g., Salaree et al., 2021). While coastal morphology is believed to be more significant on a local scale, the former has a more dominant effect throughout the propagation basin. Thus, the dominant frequency of the tsunami can be used as a first-order measure of tsunami hazard from a given source (Abe, 2006; Heidarzadeh & Satake, 2013).

The dominant frequency of fore-arc tsunamis has been shown to uniquely correspond to the fault width (the along-depth extent of faulting). In the absence of definitive constraints on the down-dip extent of ruptures in finite fault solutions (i.e., using both strong ground motion and teleseismic inversions) (e.g., Hartzell, S. H. & Heaton, 1983; Lay et al., 2010), scaling laws are often used to approximate fault dimensions (e.g., Geller, 1976; Scholz, 1982, Thingbaijam et al., 2017) and can provide estimates for fault width in the form of fractions of fault length, that is, the along-strike dimension of rupture (e.g., in Figure 1).

The dominant frequency of back-arc tsunamis, however, requires further scrutiny due to the absence of the main rupture front. Here, we first investigate the dominant frequency of back-arc tsunamis along with other source features through a physical dislocation model. We then use a large number of numerical simulations to identify the most important source parameters using synthetic as well as real data. In this regard, we consider the effects of both static initial dislocation and the transient surface waves from the mainshock. Motivated by the theoretical and numerical findings, we also evaluate the back-arc tsunami hazard in the Sea of Japan from various megathrust earthquake scenarios at the Japan Trench and the Nankai Trough. We show that considerable (∼1 m) coastal amplitudes in the Sea of Japan are possible from such back-arc events.

2. Theory and Method

2.1. Deformation Model

Coseismic deformation caused by the strain release from large earthquakes usually spreads through wide areas (sometimes hundreds of kilometers) well beyond the subduction trench (e.g., Pollitz, 1996; Chlieh et al., 2007; Pollitz et al., 2011). The deformation in back-arc regions, however, is usually difficult to constrain using seismic and geodetic data and through finite fault models due the small slip amplitudes in deeper down dip areas (e.g., Meng et al., 2011; Yokota et al., 2016). The trade-off between depth, dip angle, and seismic moment in teleseismic inversions also hinders any definite resolution of slip at larger depths (e.g., Duputel et al., 2012).

Here we use the dislocation model from double-couple solutions to model the back-arc tsunamis (see Section 6). Such models are generally known as Okada solutions of the source and approximate static deformation from inclined buried faults in elastic half-spaces (Figure 2). In contrast with finite fault models (see Section S1 in Supporting Information S1), the back-arc extension from these models is a continuation of the analytical expressions for the displacement fields of dip-slip faults. While the smooth deformation fields calculated from these models (e.g., Mansinha & Smylie, 1971; Okada, 1985) often do not consider bathymetry, the effect can be included in tsunami models by combining the horizontal component of deformation into the initial conditions for tsunami simulations (Tanioka & Satake, 1996). The Okada solutions are routinely used in tsunami simulations due to their simplicity and robustness (Okal & Synolakis, 2004; Titov & Synolakis, 1998).

Figure 2 is a simple cross-section of what we consider as the back-arc deformation model. The earthquake hypocenter and mechanism shown by a beachball is located on a fault plane depicted as an inclined, solid black line with a dip angle of δ, turning into an inclined dashed line to imply the uncertainty in the extent of down-dip rupture propagation. The deformed ocean floor (shown in orange in Figure 2) displaces a body of water from static coseismic deformation in the back-arc (shown in red). It is the geographic span and volume of this amount of water that results in back-arc tsunamis, and consequently the source parameters contributing the most to back-arc tsunamis are those increasing this volume. We note that the robustness of Okada solutions in the back-arc from double-couple centroids overcomes their disadvantages such as the neglection of rupture kinematics, due to the shortcomings of other models in constraining the downdip slip at large depths.

2.2. Tsunami Simulations

Using the calculated fields of static deformation (see Section 2.1) as initial conditions, we apply the Method of Splitting Tsunamis (MOST) algorithm (Titov et al., 2016) to simulate the tsunamis and truncate the simulations at a shallow depth (10 m) close to the shorelines to avoid nonlinear features. MOST uses the fractional steps method originally developed by Yanenko (1971) to reduce the 2 + 1 problem of solving the 2-D differential shallow water version of Navier-Stokes equations into two simultaneous 1 + 1 problems (Salaree & Okal, 2015; Titov & Synolakis, 1995).

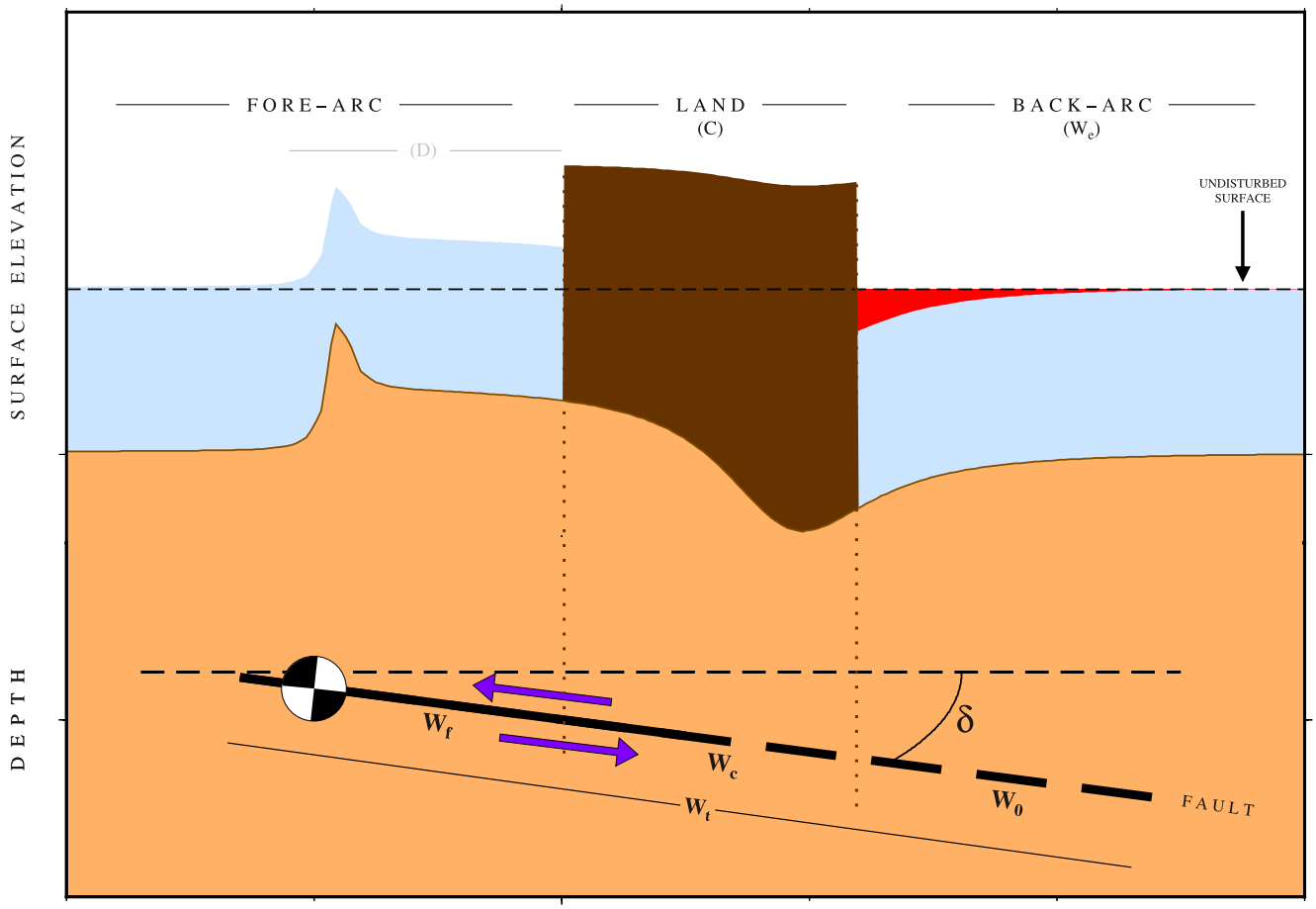

Figure 2. Along-dip cross-section of the dislocation model. Beachball represents rupture hypocenter. Purple arrows denote the down-dip fault motion. Ocean floor and water are shown in orange and blue, respectively. Back-arc displaced volume of water is depicted in red. δ represents fault dip. Definitions of length parameters are provided in Section 3.

MOST has been extensively validated and applied in tsunami studies (Synolakis et al., 2008; Tang et al., 2009; Titov & Gonzalez, 1997). Our simulations are carried out using a synthetic bathymetry grid with a resolution of 30 arc-seconds, and over 48-hr time windows with 1.5 s time steps to satisfy the CFL stability condition.

In each tsunami simulation, we record the tsunami time series at a virtual gauge in the geographic center of the back-arc basin. The dominant period is then numerically selected by carrying out a Fourier transform of the time series and picking the maxima of the amplitude spectra. In this process we avoid the very large resonance periods imposed by basin geometry through selecting an appropriate frequency range ($T < 6$ hr). We note that such long-period oscillations are expected due to the closed or open nature of the back-arc basin as well as the long (48-hr) simulation window (Section S2 in Supporting Information S1). It should also be noted that non-geometric resonance, for example, upon radiation at basin entrances (e.g., Berkhoff, 1976) and shelf overtones (e.g., Aranguiz et al., 2019) are not considered here.

3. Synthetic Experiments

3.1. Simulation Scenarios

To investigate the influence of source geometry (focal mechanism) and depth, we design deformation scenarios in a fore-arc—back-arc system as shown in Figure 2. In these synthetic scenarios, a deep fore-arc (4,000 m) is separated from a relatively shallow, closed and open (no boundaries to the north, south and east of back-arc), flat back-arc (1,000 m) by a narrow (~50 km wide) continent. The geometric setup is designed to accommodate the large width and breadth of real world back-arc basins, namely the Sea of Japan, the Caribbean, and the Gulf of

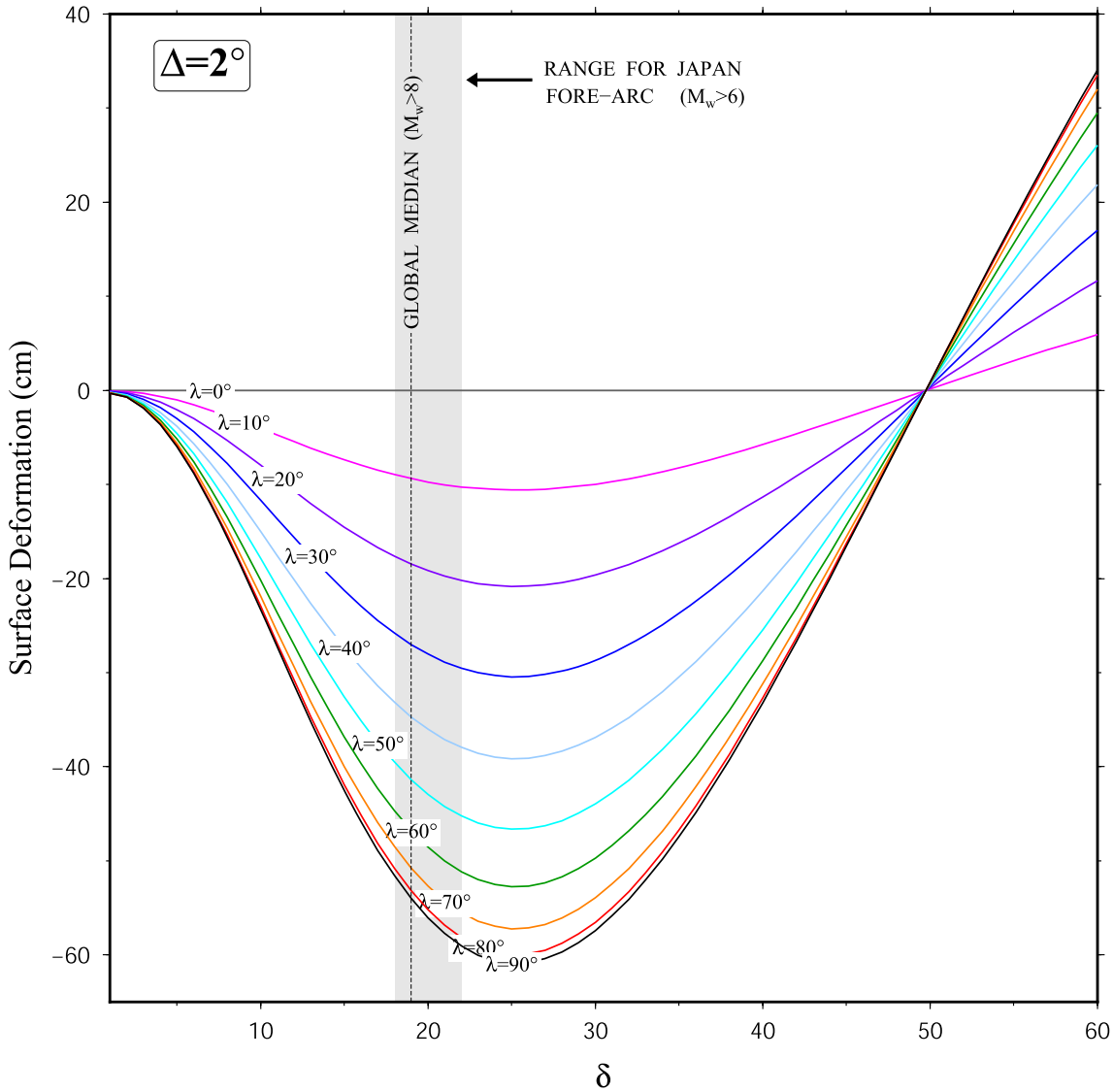

Figure 3. Calculated vertical surface deformation at a distance of $\Delta = 2°$ from the hypocenter as a function of fault dip (δ) for various slip angles (no fore-arc/back-arc systems are imposed). Calculations are carried out for a $M_w = 9$ source with a 5-km deep centroid; slip is scaled to seismic moment using Geller (1976). The vertical dashed line and the hatched area represent the global median ($M_w > 8$) and the range of dip angles for the Japanese events, respectively, from the CMT catalog.

Mexico where basin length scales exceed 15°. The closed basin was designed to test the effect of short-period basin resonance caused by internal successive reflections.

Megathrust events tend to occur in shallow depths (<40 km) with the majority of accumulated strain released within the crust and close to the trench. Based on our dislocation model (Figure 2), earthquakes with larger seismic moment (i.e., larger ruptures) or those closer to the continental arc are naturally expected to create larger back-arc tsunamis as they would displace more water on the opposite side of the continent. However, as large ($M > 8.0$), shallow megathrusts capable of generating large back-arc tsunamis tend to occur at or in the vicinity of trenches, the most loosely constrained source parameter will be the source geometry instead of location. Although as a global average, trenches are located ~250 km away from continents, depending on the shape, size, and physical properties of the megathrust zone, these ruptures can take place only slightly closer to land (Bilek & Lay, 2018). Therefore, the magnitudes of megathrusts also determine the extent of down-dip faulting and thus that of back-arc deformation (see Figure 2).

While larger dip angle of source ruptures would result in more significant vertical components of initial deformation, and thus larger tsunamis at least in the near-field as shown in Figure 3 (e.g., Gica et al., 2007; Titov

et al., 1999), megathrusts tend to occur at shallow dips ($\delta < 30°$) and with slip vectors almost perpendicular to the trench ($45° < \lambda < 135°$). In fact, the global median of dip angles for $M_w > 8$ events from the CMT catalog is $\delta \approx 19°$ (the vertical dashed line in Figure 3).

One can show that meaningful back-arc deformations in this setup would only occur for megathrust events and thus we set a $M_0 = 1.3 \times 10^{28}$ dyn-cm ($M_w = 8.0$) as the minimum seismic moment in our designed scenarios. We also set $M_0 = 2.2 \times 10^{30}$ dyn-cm ($M_w = 9.5$) as the high end of rupture moments. The latter moment may be excessive but is chosen to accommodate the worst-case scenario (as was the case during the 20 May 1960 M9.5 Chilean rupture).

By taking these geometric constraints into account, we design a large number of synthetic scenarios by placing source centroids in the fore-arc, 75 km away from the continent at a central latitude (representative of arc systems with narrow continents and high potential of back-arc tsunamis, e.g., Oaxaca). Each scenario is designed as a set of (M_w, H, δ, λ) (i.e., magnitude, centroid depth, dip, and slip) with $8.0 \leq M_w \leq 9.5$, 10 km $\leq H \leq$ 40 km, $10° \leq \delta \leq 40°$, and $40° \leq \lambda \leq 90°$ (benefiting from the axial symmetry along latitude) while keeping the rupture strike the same as that of the trench, assumed to be parallel to the continental arc (see Table S1 in Supporting Information S1). The choice of depth range is valid due to the nature of centroids and has been documented for large megathrust events in the past (e.g., the 2011 Japan (Ide et al., 2011)). We then calculate static deformation fields based on the algorithm by Mansinha and Smylie (1971) as a type of Okada algorithms using earthquake scaling laws for uniform slip (Geller, 1976; $M_0 = 1.45 \times 10^{20}.\Delta\sigma.L^3$ with $\Delta\sigma$ and L as a constant stress drop and fault length where the fault length is related to its width W by $L = xW$ where x depends on earthquake magnitude, etc). Under scaling laws, earthquake dislocation (regardless of source parameters, e.g., focal geometry, depth, etc) are invariant of stress drop, and assuming constant rigidity, of strain release (Okal & Synolakis, 2004). The scaling leads to approximations for fault dimensions and slip which have been extensively benchmarked using large datasets of earthquakes and tsunamis (e.g., Thingbaijam et al., 2017). In these simulations, by choosing centroid over hypocenter, we have ensured that the ruptures do not breach free surface, hence abiding by the requirements of Okada algorithms. Besides, by confining the fault width within the global depth of the seismogenic zone for megathrusts, that is, 40 km, we have avoided unrealistic faulting.

3.2. Simulations

We use these scenarios to simulate back-arc tsunamis using the strategy described in Sections 2.2 and 3.1. Examples of these scenarios and their simulation results are shown in Figure 4. The left panels in Figure 4 (Figures 4a and 4b) show the initial deformation fields calculated for $M_w = 9.0$ scenarios with constant depth and slip angle ($\lambda = 90°$) and at two different dip angles ($\delta = 10°$ and $\delta = 20°$). The middle panels (Figures 4a' and 4b') show the simulated maximum tsunami amplitudes from the two scenarios in Figures 4a and 4b. The spectra for the simulated tsunamis in closed and open back-arc basins are shown in Figures 4a" and 4b" as blue and red curves, respectively. Dominant periods from simulations are depicted by red, dashed lines.

Similar comparisons can be drawn for other designed scenarios with different parameters (i.e., seismic moment, focal depth, and slip angle) as shown in Figure 5. The double-primed panels in Figure 5 show the spectra of the time series from virtual gauges (yellow stars) in each corresponding scenario shown on the left. The blue and red curves in these panels belong to simulations in closed and open (back-arc basin is not bounded) back-arc basins. We can see in Figure 5 that the spectral contents of the closed and open cases in each scenario are very similar with the closed cases behaving as a discretized version of the open counterparts. Meanwhile, the similar dominant periods across the two suggest that basin properties come second to earthquake source properties in affecting the back-arc tsunami spectra. We note that the virtual tide gauge used in the spectral analysis is placed at the geographic center of the basin (yellow stars in Figures 4 and 5), far from the boundaries and significant, static deformations (from source) and is thus a good measure of the tsunami propagation. We attribute the beating spectral nature of the tsunami in closed back-arc basins to the oscillatory modes from multiple reflections of hydrodynamic standing waves. Due to the spectral similarity of closed and open cases in each scenario, as well as the smoother nature of the spectra in the open case, we will focus on the latter as the representative for back-arc tsunamis in the rest of the paper.

It is readily seen in our simulation results (Figures 4 and 5; also see Table S1 in Supporting Information S1) that similar to the far-field manifestation of their shallow, fore-arc counterparts (e.g., Ward, 1980), the effect of centroid depth on back-arc tsunamis is not significant (e.g., note the differences between Figures 4b and 5d as

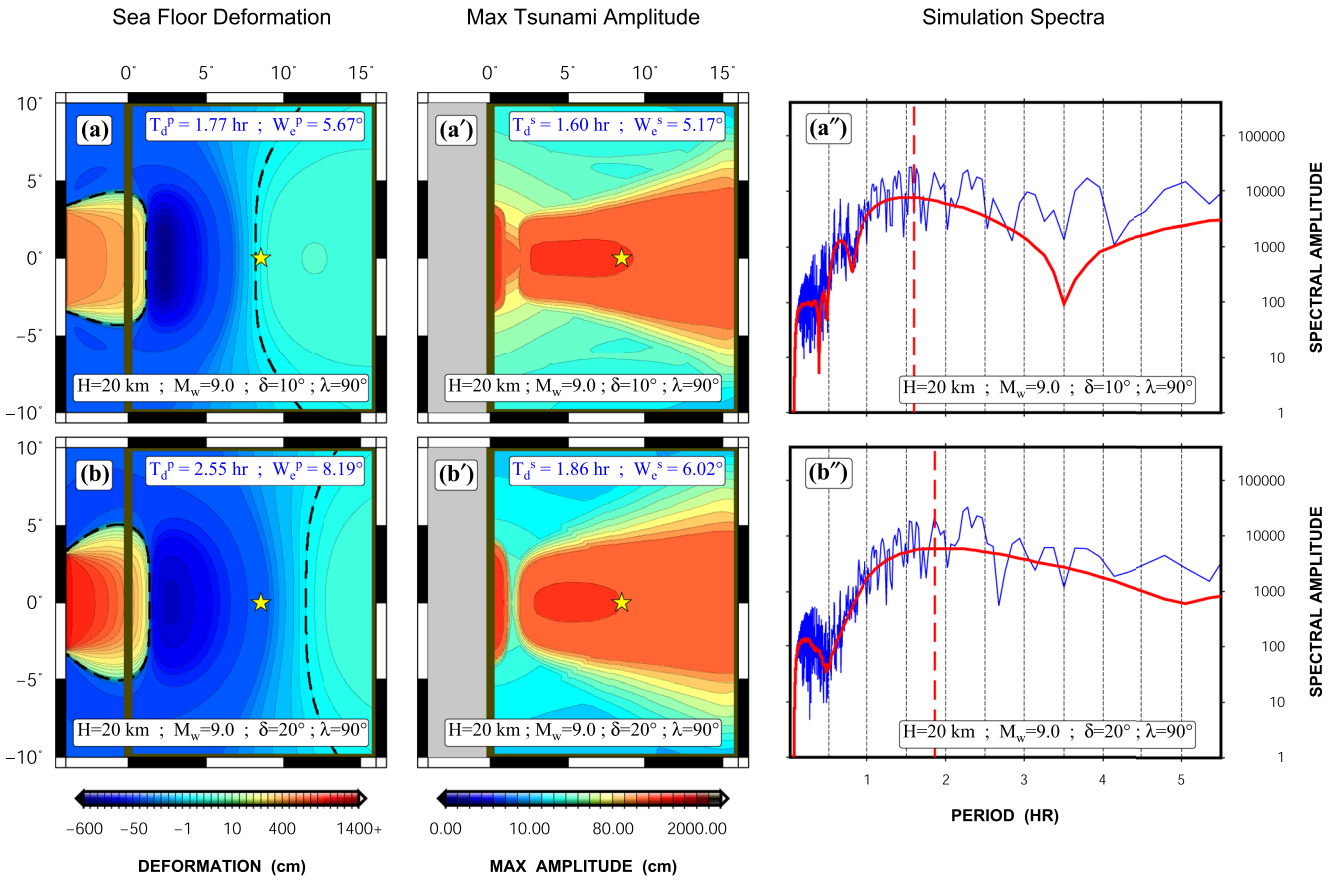

Figure 4. (a, b) Ocean floor deformation fields calculated from M_w 9.0 point sources in the fore-arc for two dip angles (10° and 20°). Black, dashed lines show the deformation nodes (i.e., zero deformation). In each panel, dominant tsunami periods from numerical simulations (T_d) and the corresponding length scale (W_e) to those periods are listed. The "*p*" and "*s*" superscripts denote values predicted from our model, and those from hydrodynamic simulations, respectively (see Sections 3.1 and 3.2). (a', b') Simulated maximum tsunami amplitudes from the scenarios in (a and b). Fore-arc values are masked in gray to focus on the back-arc tsunami. (a", b") Spectra of the simulated tsunamis at virtual gauges (yellow stars) in each corresponding scenario in (a and b). The blue and red curves are from scenarios with closed and open back-arc basins, respectively. Red, dashed lines show spectral maxima of the red curves. Time series for the virtual gauges are shown in Fig.

well as their primed and double-primed counterparts). In comparison with the effect of varying depth, changing the slip angle (λ) leads to a more significant change in the back-arc propagation pattern, and the metric MT as a measure of difference between tsunami propagation maps has a value three times larger between Figures 4b' and 5c' than that between Figures 5c' and 5d' (MT = 9.8×10^{-6} compared to MT = 2.9×10^{-6}). Among all the source parameters tested in the dislocation models, variations in dip angle (δ) cause the largest changes in the back-arc tsunami, for example, MT = 1.1×10^{-5} between Figures 4a' and 4b'. We recall that MT is a pointwise comparison metric for two congruent tsunami propagation maps, and that smaller values of MT correspond to more similar propagation fields (Salaree & Okal, 2020).

Our simulations of back-arc tsunamis in these synthetic scenarios show larger tsunami amplitudes at higher dip angles, similar to their fore-arc counterparts (Figure 6). This is due to the increase in the deformation amplitude at higher dip angles ($\delta \leq 45°$) (Figure 3). We attribute the decrease in maximum tsunami amplitudes at higher dip angles for smaller sources (M_w = 8.0 and 8.5) in Figure 6 to the transition of significant deformation values from the back-arc basin under the continental arc. This results in the exclusion of the corresponding initial conditions from tsunami simulations.

Our results also show that contrary to fore-arc tsunamis, the back-arc dominant period is not constant, that is, not uniquely determined by fault width (Rabinovich, 1997). In Figure 5a"–5d", dominant periods are picked as the maxima of the computed spectra (shown by vertical, red, dashed lines). We note that, as expected, seismic moment is the main factor affecting the dominant period of back-arc tsunami (e.g., see Figure 5b" and Table S1 in Supporting Information S1), but we find the dominant period also varies with the dip angle of the fault plane.

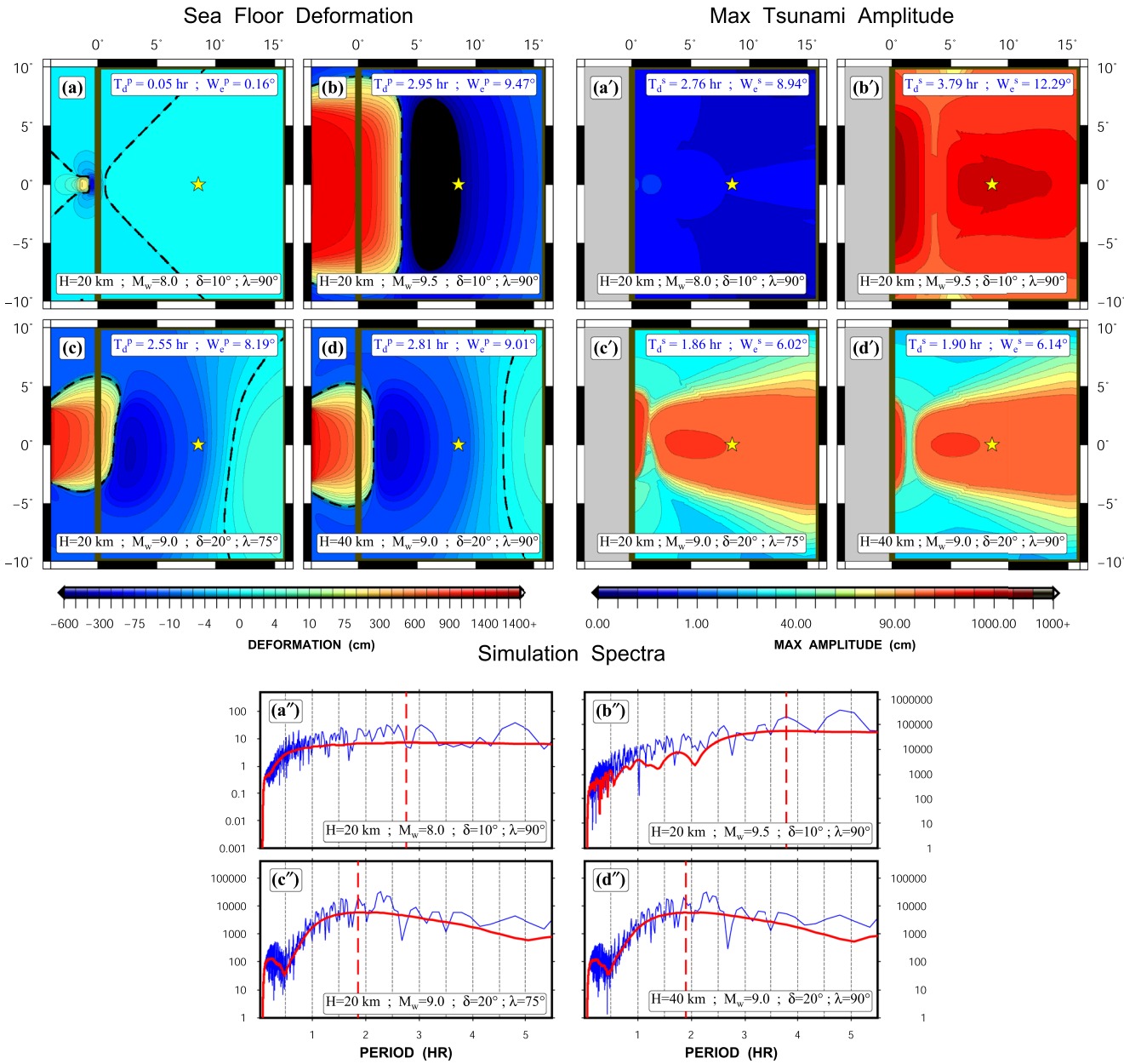

Figure 5. Similar to Figure 4, but for scenarios with different geometries and sizes. Note the different vertical scales across (a"–d").

3.3. Dipping Plane Model

Our observations can be explained by studying how seismic moment and dip angle of the rupture would affect the extent of back-arc deformation. In the absence of the main, fore-arc rupture front, one can model the horizontal extent of negative polarity surface deformation in the back-arc as the projection of the fault plane on the far side of the continental arc onto the surface (Figure 7). In this formalism, seismic moment, and thus the along-dip length of the fault plane is the main factor affecting the horizontal length scale or *effective width*, W_e, of surface deformation. Also, dip angle (δ) affects W_e upon projecting the actual fault width, W_0, to the surface in the form of $W_0 \cos\delta$. Determining the back-arc source depth is a more complex issue in this model as it is expressed in the form of a secondary depth, that is, H_e in Figure 7, which is related to the centroid depth, H_0, as $H_0 + W_0 \sin\delta$ where δ is the dip angle. From the tsunami point of view, in the absence of a fixed point as hypocenter or centroid in the back-arc, this quantity is not constant and varies along the downdip plane.

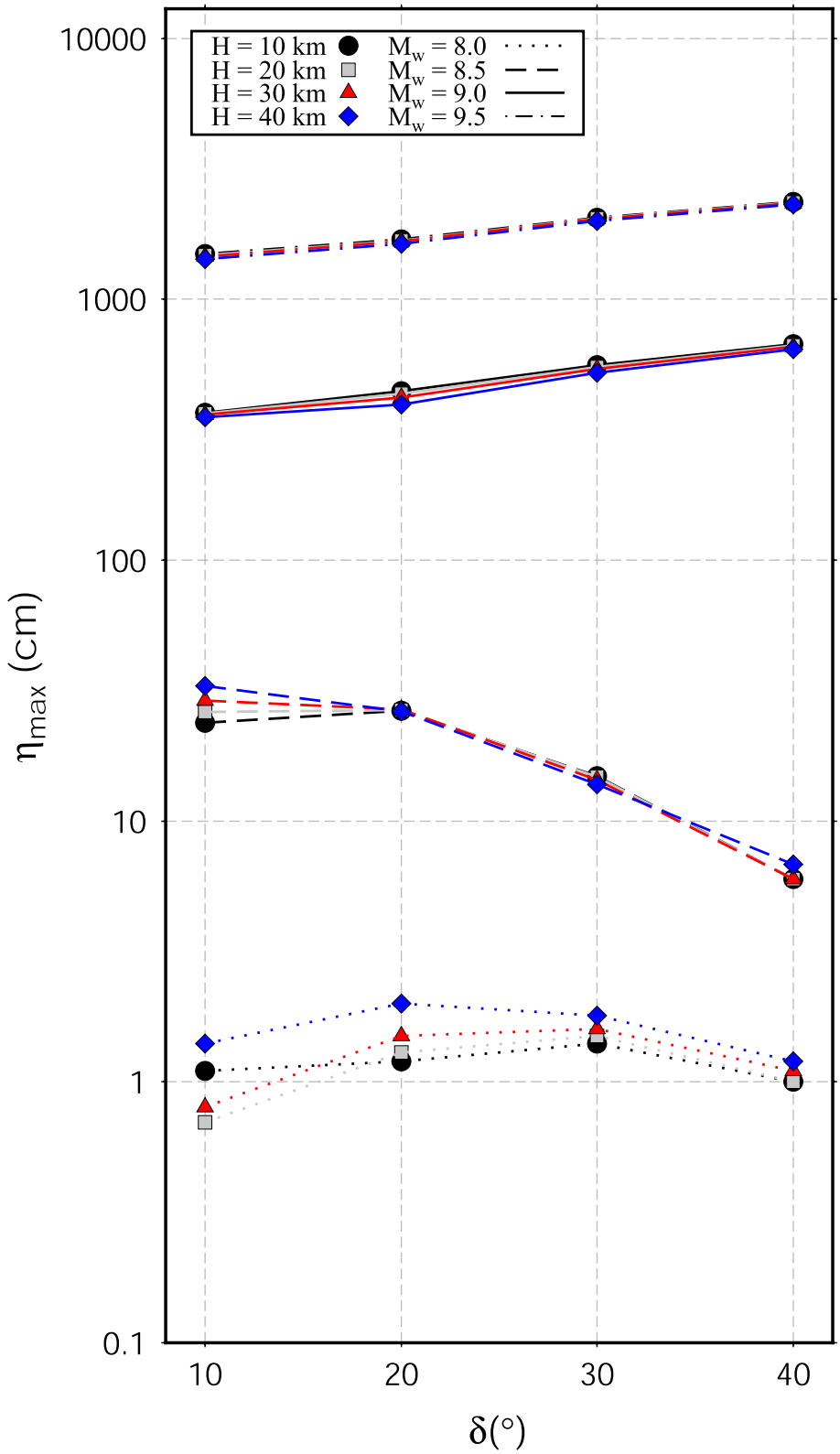

Figure 6. Variations in maximum back-arc tsunami amplitude, η_{max}, as a function of dip angle (δ), centroid depth (H) and moment magnitude. Colors and patterns of each curve represent different depths and magnitudes.

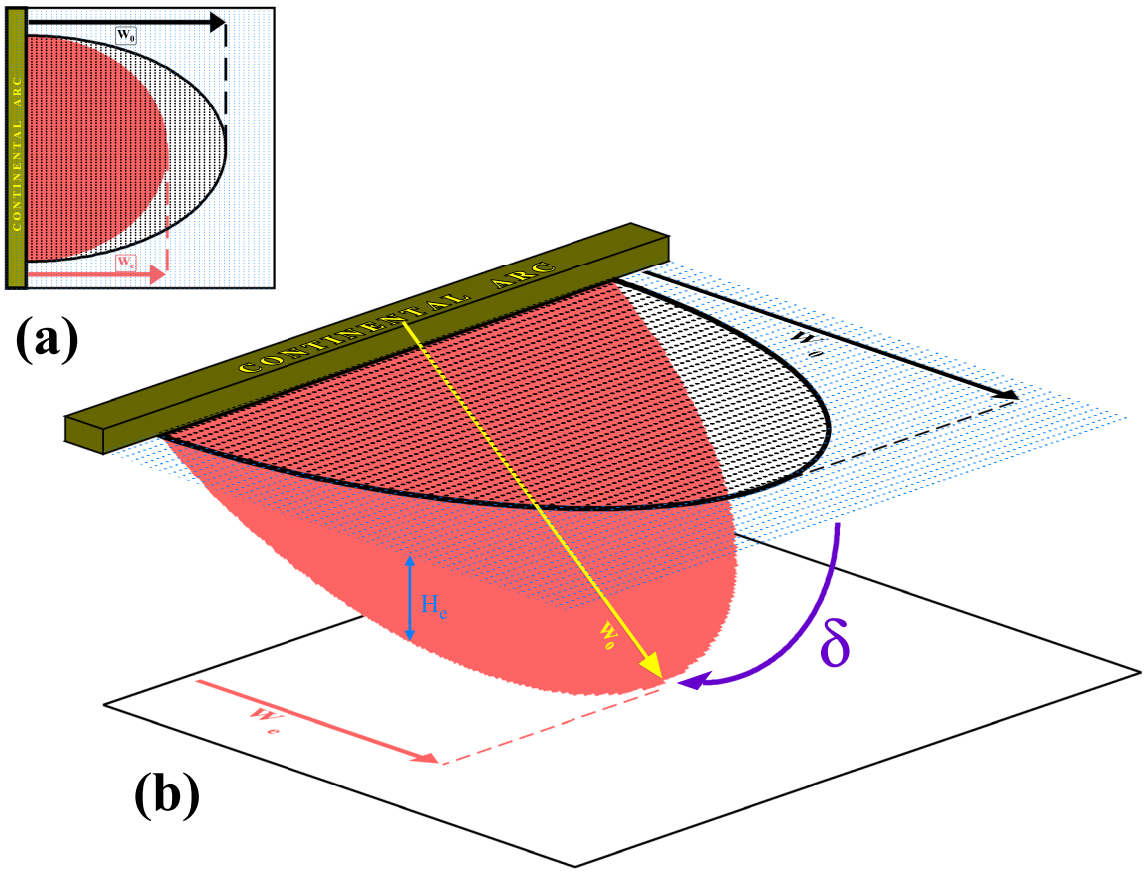

Figure 7. (a) Map view and (b) side view of the surface projection of rupture plane onto the surface. H_e, W_0 and W_e are the contribution of rupture in the back-arc (i.e., effective depth) to apparent depth, width of rupture plane in the back-arc, and effective width of the rupture. δ represents fault dip.

We note that the total fault width (W_t) as inferred from teleseismic data is the sum of fore-arc, subcontinent, and back-arc along-dip segments of the fault plane as depicted in Figure 2 by W_f, W_c, and W_0, respectively:

$$W_t = W_f + W_c + W_0 \tag{1}$$

or,

$$W_t = \frac{1}{\cos\delta}(C + D + W_e) \tag{2}$$

where C represents the width of continental arc, and D is the trench-to-continent distance (see Figure 2).

We can use this model to predict the dominant period of back-arc tsunamis, by measuring the largest distance between successive maxima and minima in the zero-latitude cross-section of back-arc deformation, as shown in Figure 8 which is equivalent to the effective width in our model. We note that Figure 8 shows narrow sections at zero latitude in the deformation fields and thus the lack of symmetry in the non-pure mechanisms ($\lambda \neq 90°$) does not impose an issue to our simple model. For each source scenario (e.g., the panels in Figure 8) we can compute a corresponding dominant period using the measured effective width (W_e) and the group velocity of tsunami from shallow water approximation ($c = \sqrt{gh}$). The latter is valid due to the large length scale of the back-arc source and the shallow (1,000 m) flat ocean (for effects of slip angle, see Section S3 in Supporting Information S1).

This model predicts larger dominant periods for the back-arc tsunamis at larger dip angles (see Section 6 for the discussion of mismatch), in agreement with the results from our hydrodynamic simulations, as shown in Figure 9. The effective width in this simple model explains the quadratic fits to the calculated dominant periods at various dip angles in Figure 9 as they can be thought of Taylor expansions with small quadratic coefficients of the cosine function (Equation 2). It is noteworthy that Equation 2 provides a proxy to constraint the down-dip extent of rupture upon measuring the dominant period of back-arc tsunami, and hence estimating the total width.

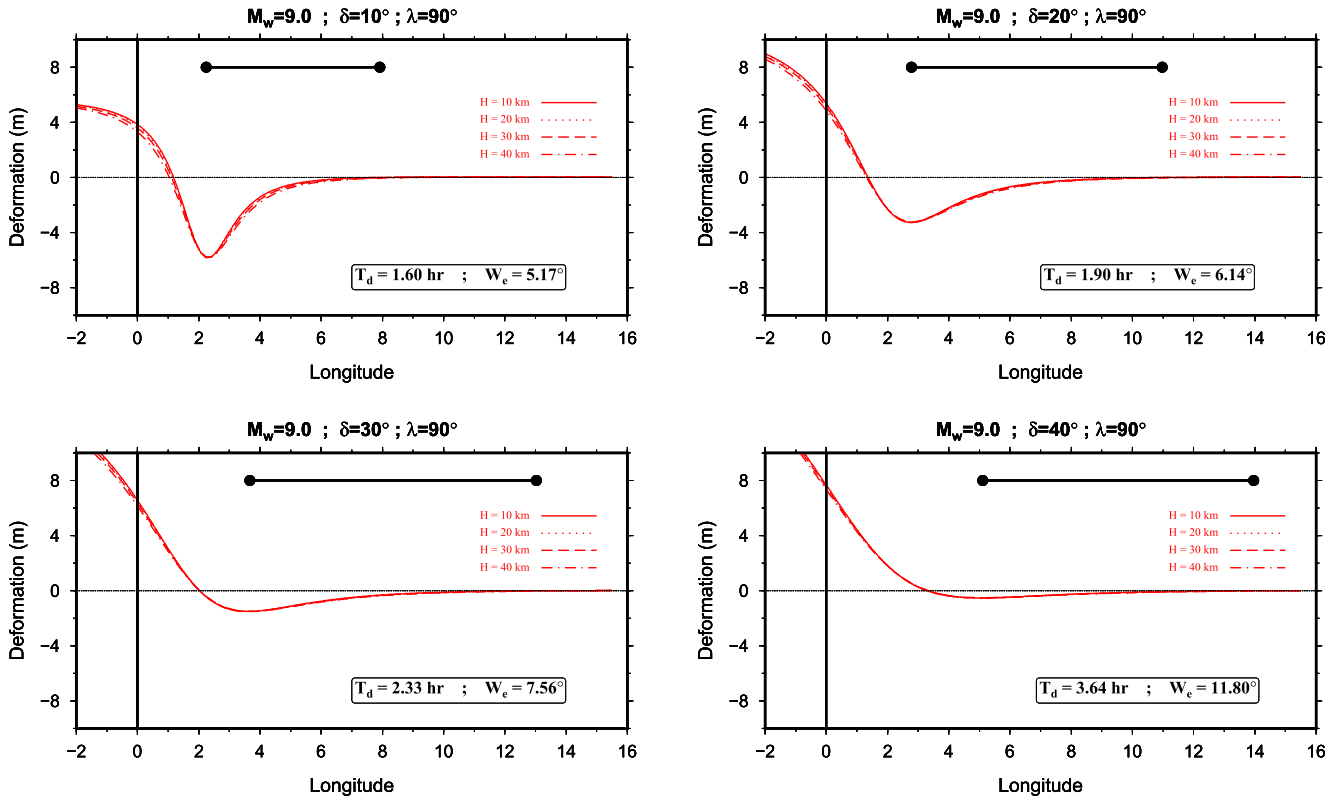

Figure 8. Measuring effective widths (black, horizontal lines) at various dip angles as the largest distance between successive maxima and minima in the cross-section of back-arc deformation. The panels show cross sections from four scenarios with different dip angles at $\lambda = 90°$. Red curves in each panel represent scenarios with various centroid depths. Dominant periods, T_d, are calculated from their corresponding effective widths, W_e.

As shown in Figures 4, 5, and 9, our model provides a reasonable estimate of the back-arc spectral maxima across various dip angles for the $M_w = 9.0$ scenarios. We attribute the disagreement between the predicted and simulated dominant periods of back-arc tsunamis for $M_w = 8.5$ and $M_w = 9.5$ (scenarios compared to the $M_w = 9.0$) to the deviation of deformation fields from our proposed model. In the $M_w = 8.5$ scenarios, a considerable part of negative polarity deformation is located in the fore-arc (as W_f and W_c) and hence does not contribute to the back-arc tsunami. At the other end, vast positive deformation parts of the significantly larger $M_w = 9.5$ source leak into the back-arc, thus violating our assumption of negative-only deformation in our simple model (see Figures 2, 5b and 7). In other words, in $M_w = 8.5$ and $M_w = 9.5$ scenarios, we are respectively undersampling and oversampling the back-arc source deformation. We note that the positioning of our source scenarios is constrained by physical and tectonic properties of the back-arc basin and location of trench. This inevitably results in deviations of simulation scenarios from our simple theoretical model. Figure 10 demonstrates how the width of continental arc can affect the working threshold of our model. In Figure 10, various widths of the continental arc result in different polarities of deformation to be exposed or hidden from the back-arc basin. For instance, while in a 50 km wide arc (i.e., our simulations) an $M_w = 8.7$ source is the ideal scenario for our model, for an $M_w = 8.9$ event a 200 km wide arc in our model works best. Finally, we attribute the under- versus overestimation of back-arc amplitude by our model to the nonuniform trigonometric projection of fault plane to the surface, as well as the expressions of the nonlinearity in the Navier-Stokes equations which is missing from our models.

These results show that the back-arc tsunami hazard is dominated by earthquake magnitude and the dip angle of the fault plane. In fact, our simulations show that a magnitude 9.0 earthquake can result in back-arc tsunamis reaching ~1 m amplitudes (Figure 6). At the same time, larger tsunamis are expected for sources with larger dip angles, and that these tsunamis have a lower frequency content (red-shifted) resulting in less energetic tsunamis. We note that while we have carried out our simulations in ideal, flat back-arc basins, the presence of complex bathymetric features would complicate the propagation of these tsunamis. Also, the abundance of concave coastal morphology in the far side of continental arcs is expected to increase the back-arc coastal tsunami amplitudes.

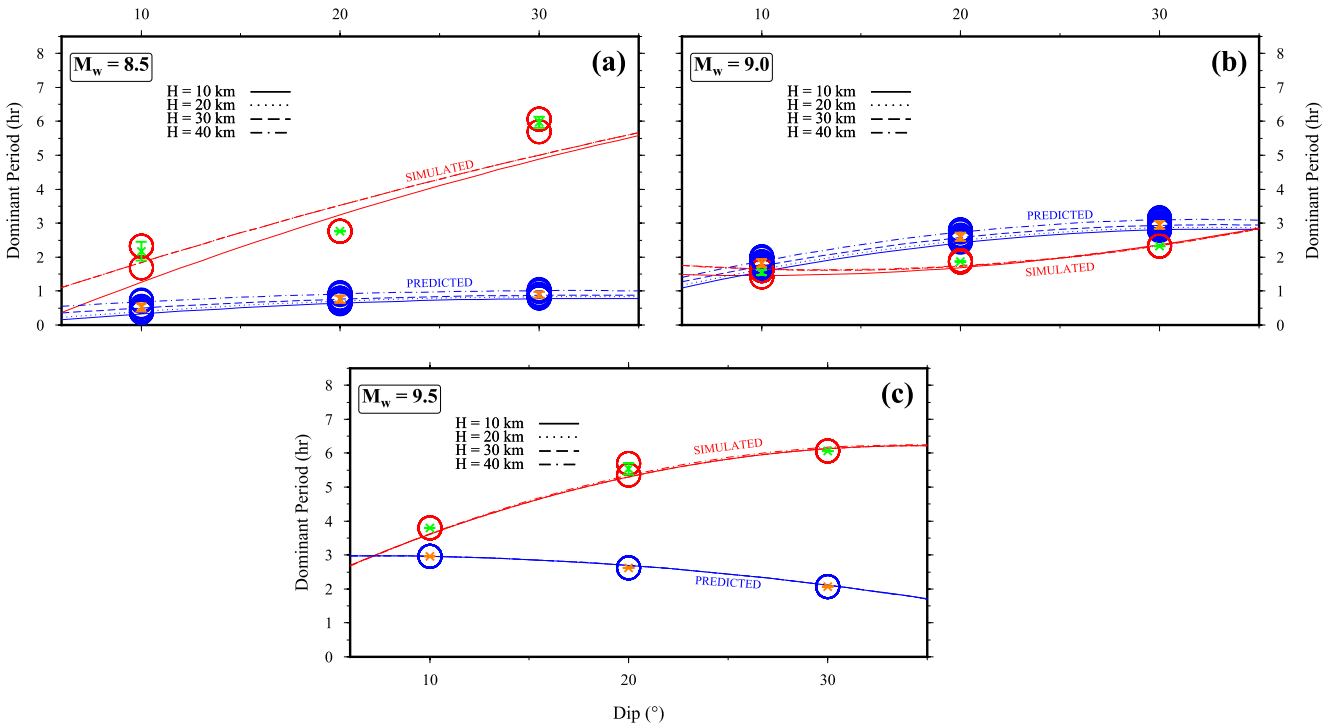

Figure 9. Variations in back-arc dominant period as a function of changes in dip angle from four source scenarios with different magnitudes. In each panel, blue and red circles represent respectively predicted and simulated dominant periods for various centroid depths. Orange and green vertical lines are error bars at each dip angle for the predicted and simulated groups, respectively. The shown curves are quadratic fits to each depth scenario.

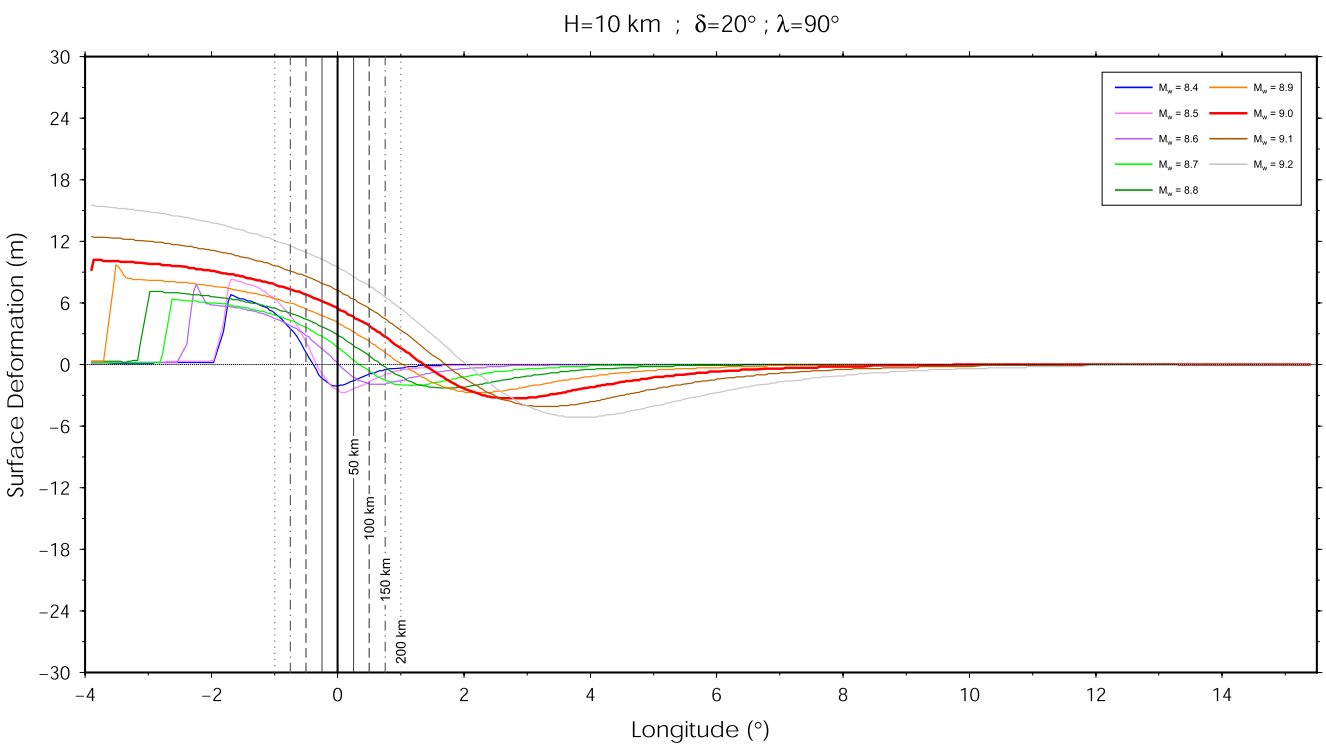

Figure 10. Deformation profiles from 8.4 ≤ M_w ≤ 9.2 earthquakes (at 0.1 magnitude increments) throughout the fore- and back-arc domains. The vertical lines depict continental arcs with various total widths, labeled in km.

With these points in mind, we proceed to investigate the back-arc tsunami hazard in the Sea of Japan where there has been a well-documented example of back-arc tsunamis in the past.

4. Back-Arc Tsunamis in the Sea of Japan

Here, we use our findings from Sections 2 and 3 to obtain a better understanding of back-arc tsunamis in the Sea of Japan. The Japan Trench has hosted the 2011 $M_w = 9.0$ Tohoku rupture, one of the largest recorded earthquakes in the instrumental era. At the eastern margin of the Japanese Islands, the convergence between Pacific and Okhotsk plates has resulted in an active subduction which has experienced numerous megathrust earthquakes and therefore tsunamis in the past (e.g., Hashimoto et al., 2009; Satake, 2015). Similarly, in the south, the subduction of Philippines plate under the Eurasian plate has generated a rich history of large earthquakes along the Nankai Trough (e.g., Ando, 1975; Ishibashi, 2004; Yokota et al., 2016).

Both the aforementioned subductions have created M9 earthquakes and larger in the past and are expected to do so in the future. Therefore, the excitation of back-arc tsunamis from any such event needs to be considered while studying the tsunami hazard in the Sea of Japan.

4.1. The 2011 Tohoku Earthquake and Tsunami

The 2011 M_w = 9.0 Tohoku earthquake created perhaps the best recorded back-arc tsunami to this date, mainly due to the dense population of tide gauges all around the Sea of Japan. This earthquake ruptured a ~200 × ~400 km patch of the Pacific-Okhotsk plate boundary along the Japan Trench (Ammon et al., 2011; Ide et al., 2011; Lay, 2018; Shao et al., 2011) with unusually large slip, up to 50–80 m (Fujiwara et al., 2011; Ito, Osada, et al., 2011). The shallow CMT hypocenter at ~25 km combined with the large slip resulted in large values of ocean floor uplifts of near the coastline, as well as ~30 m vertical and ~60 m horizontal displacements at the trench, respectively (Ito, Ozawa, et al., 2011; Kido et al., 2011). The large areas of uplift and subsidence at the ocean floor (Grapenthin & Freymueller, 2011) generated a devastating tsunami reaching 40 m along the Sanriku coast (Mori et al., 2011; Shimozono et al., 2012).

However, the coseismic deformation was not limited to the trench side of the Japan island—the fore-arc. In fact, geodetic measurements documented decimetric and centimetric deformations in the western Japanese coastlines (Pollitz et al., 2011). This so-called back-arc field of deformation would continue into the Sea of Japan and result in a complex pattern of uplift and subsidence at the sea floor. Numerical models also successfully predict centimetric deformation westward across the Sea of Japan reaching Russia (Pollitz et al., 2011; Sato et al., 2011). Such back-arc deformations are expected from our models based on the Okada solutions (Figures 1 and 2). The resulting moderate back-arc tsunami was recorded by tide gauges all around the Sea of Japan including in Japan, Korea and Russia.

4.2. Tide Gauge Data

To investigate the propagation of the 2011 back-arc tsunami, we use data from three tide gauges along the western coastlines in Rudnaya Pristan, Preobrazheniye (both in Russia), and Busan (Korea), as well as five tide gauges from Geospatial Information Authority of Japan (GSI) on the Japanese coast (Figure 11a). These stations provide a reasonable azimuthal coverage of the tsunami around the Sea of Japan. The Busan station is used to analyze the critical interaction of fore- and back-arc arrivals. The time series from the Russian and Korean sites are sampled at 1-min, and Japanese data are sampled at 30-s intervals. The data is de-tided by applying a 6-hr filter which (as discussed in Section 2) also helps with removing the effects of basin-wide resonance.

4.3. Contribution of Surface Waves

Upon modeling the 2011 back-arc tsunami, Murotani et al. (2015) expressed concern regarding the match between tide gauge data and their simulations at high-frequencies. To investigate this issue, we also include the contribution of seismic surface waves to tsunamis which can affect the higher end of the frequency content of tsunamis due to their high amplitudes and wide spectral range (Barberopoulou et al., 2004; Saito et al., 2019). Our simulations consider the initial deformation from Rayleigh waves which typically possess higher frequency

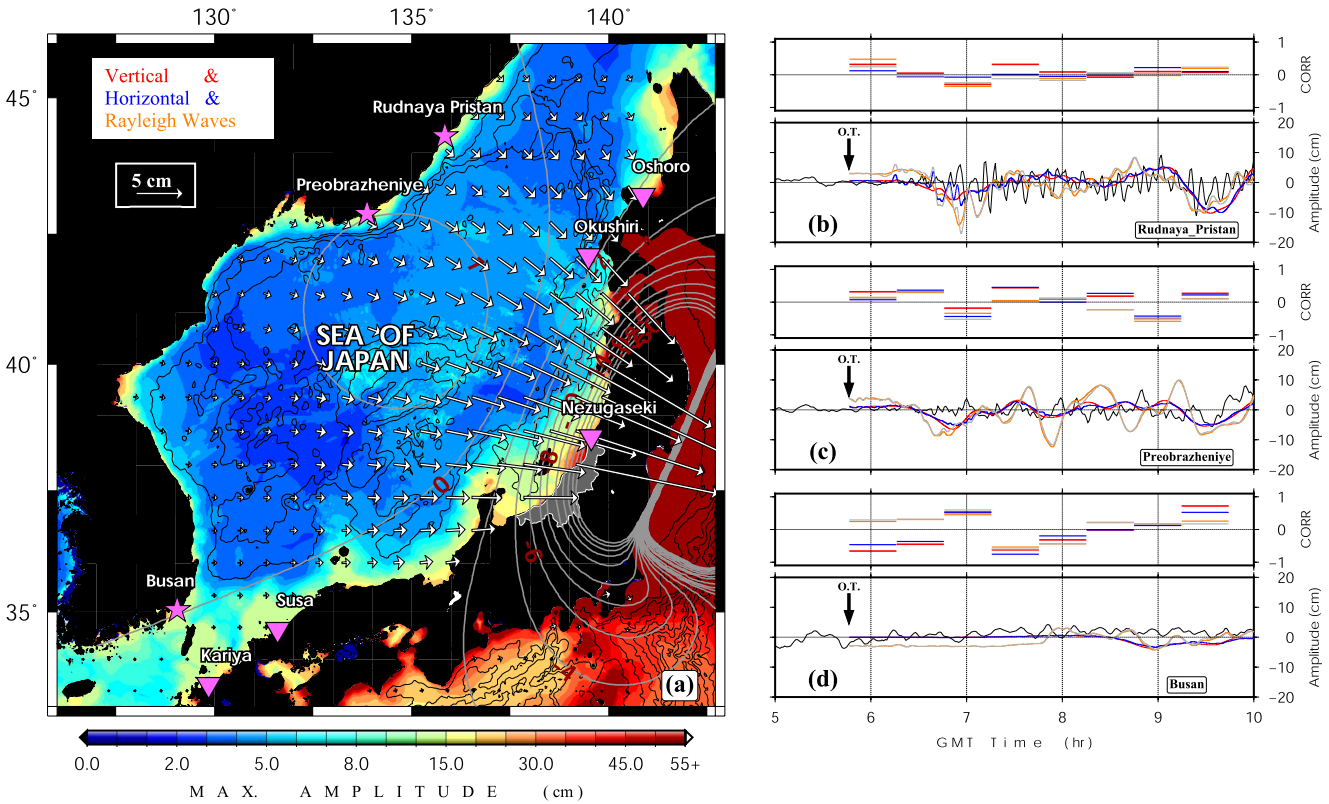

Figure 11. (a) Simulation of the tsunami in the Sea of Japan from the 2011 Tohoku earthquake using both vertical and horizontal components of static deformation from the CMT source as well as the Rayleigh waves. Gray contours represent the vertical static deformation, labeled in centimeters. Arrows are scaled to the horizontal component of deformation field. The Niigata Prefecture (the location of largest reported waves) is shown as a shaded part of western Japan. (b—d) Tide gauge records from the 2011 Japan tsunami at three locations: (b) Rudnaya Pristan, (c) Preobrazheniye, and (d) Busan, also marked in (a). Recorded data is shown by a black curve. Simulation results at these locations from various scenarios in are shown in different colors: vertical deformation only (red), vertical and horizontal deformation (blue), vertical deformation and Rayleigh wave (orange), and all three (gray). Rupture origin time is marked with black arrows. Top panels show correlation coefficients of each simulated time series with the recorded data in 30-min intervals.

content than the longer period tsunami waves. Using a normal modes approach, we calculate surface wave eigenfunctions down to ~150 s (see Section S4 in Supporting Information S1). This corresponds to a spatial resolution of ~30 km in the Sea of Japan, which is shallower than 4,000 m, and should be sufficient considering the large source dimensions.

4.4. Simulation of Tsunamis in the Sea of Japan

We carry out tsunami simulations in the GEBCO bathymetric grid with a spatial resolution of 30 arc-seconds (Weatherall et al., 2015) using (a) vertical deformation, (b) both vertical and horizontal deformations for the CMT solution, and (c) a combination of surface deformation and Rayleigh waves (more details are shown in Supporting Information S1). Simulations cover the geographic window of 124°–150°E and 28°–46°N and a 48 hr time window after the rupture origin time and use 1.5 s time steps to satisfy the CFL condition. While our virtual gauges are often placed at a distance of several kilometers from shorelines, we terminate the computations at the depth of 10 m to avoid nonlinear effects including those caused by harbor resonance (similar to the strategy in Section 2.2).

Figure 11a shows the simulation result from the superposition of all three deformation sources as initial conditions. Each panel in Figures 11b–11d shows the simulated time series compared to recorded data (black curves) as well as their correlation coefficients (CC) for 30-min time intervals (see Sections S5 and S6 in Supporting Information S1 for the longer time series). Variations in the calculation intervals for CC shows that 30 min is an approximate threshold after which the rate of change in CC as a function of calculation interval decreases. The

choice of CC over amplitude matching is due to the fact that CC is a better representation of variations in signal's trend (i.e., period). Also, the large-scale apparent amplitude mismatch (Figure 11) is likely caused by our simple uniform-slip source model which does not incorporate the variations in down-dip moment release (Kanamori et al., 2019).

Similar to this study, Murotani et al. (2015) were more successful in matching the observed signals from stations at the far side of the Sea of Japan. The discrepancy near the coast of Japan is possibly due to the effect of bathymetry caused by the horizontal component of deformation. We attribute the practically non-existing coseismic amplitudes and the signal complexity in Busan (similar issues can be seen at Okushiri in the north) to its proximity to the deformation node (Figure 11a). Beamforming of tsunami waves in the Korea Strait shows that the slower back-arc waves (from the shallow continental shelf) arrive at Busan only slightly earlier than the faster fore-arc waves (from the deep trench). The flip-flops in the dominant azimuth of arriving tsunami waves near Busan shows significant changes in the propagation direction as well as the influence of large-scale reflections (Section S7 in Supporting Information S1). Thus, the first arrival is an emergent phase with negative polarity (edge waves from the nearby coseismic coastal depression in the back-arc). Later on, this signal mixes with the positive polarity, fore-arc signal in a complex pattern, hence resulting in the poor fit of the simulations. This underlines the importance of source geometry in excitation of back-arc tsunamis.

Murotani et al. (2015) and Kim et al. (2019) both concluded that bathymetry plays a significant role in the higher frequency content of back-arc tsunamis. This effect is more noticeable in the presence of smaller deformation, for example, in the case of Busan where the 2011 tsunami arrived more than 1 hour later than the Russian sites (Figures 11b–11d). Ray-tracing experiments confirm that the Japanese sites as well as Busan experience considerably more complex wavefronts than those on the far side of the Sea of Japan, due to the entrapment of tsunami energetics in the complex southern bathymetry (Section S8 in Supporting Information S1). Our results show that the contribution of Rayleigh waves to the 2011 Tohoku back-arc tsunami at locations in the intermediate-field may be important, as their addition slightly improves fits to the observed signal (~30% increase in CC) at higher frequencies (during the first few minutes of the records after origin time) in Rudnaya Pristan but not in Preobrazheniye (Figure 11b). While these stations are approximately in the same radiation Rayleigh lobes, it seems that the interaction of surface waves with bathymetry complicates their contribution as is the case with Preobrazheniye. This probably led to the higher frequency content of the signal in Rudnaya Pristan tide gauge data (see Section S9 in Supporting Information S1). In fact, by dividing the back-arc deformation into near- and far-field components (near Japan and Russia, respectively) we can show that the high-frequency part of the record at Rudnaya Pristan can be better reproduced by considering only the far-field component, while the near-field deformation which is farther from the recording station provides a better match of amplitudes as well as the longer-periods in the data (Supporting Information S1).

5. Potential Back-Arc Tsunami Hazard in the Sea of Japan

We use the proposed rupture locations and geometries from previous studies as potential future sources that are large enough to produce back-arc tsunamis in the Sea of Japan. Here, we do not include surface waves in the simulations as our results from Section 4 showed their contribution may be significant only in the presence of simple bathymetry, that is, the shallow northwestern (Russian) side of the Sea of Japan where the tsunami will be attenuated faster. Our choice is also based on the fact that we are mainly investigating the largest amplitudes, not the first, high frequency portion of tsunamis in order to provide estimates of the back-arc hazard. Also, for the hypothetical and speculative scenarios in Sections 5.1 and 5.2, inclusion of the unconstrained surface waves without observational basis is likely to result in systematic accumulation of errors and unrealistic tsunami amplitudes.

5.1. Japan Trench

A successive cascade of ruptures on the fault patches at the Japan Trench can occur during a single large megathrust (e.g., Satake, 2015), similar to the 2011 Tohoku event (Noda & Lapusta, 2013; Stein & Okal, 2011). As a given paleoseismic window may not capture long-term trends in seismicity (Salditch et al., 2020), such large rupture areas can be keys to understanding the maximum possible earthquake and tsunami hazards.

We construct a composite rupture area by joining the previous M_S 7.1–7.8 events in 1936, 1937, 1938, and 1978 in the Miyagi-oki sequence, spanning a total geographic area of ~300 × ~150 km (Abe, 1977; Satake, 2015;

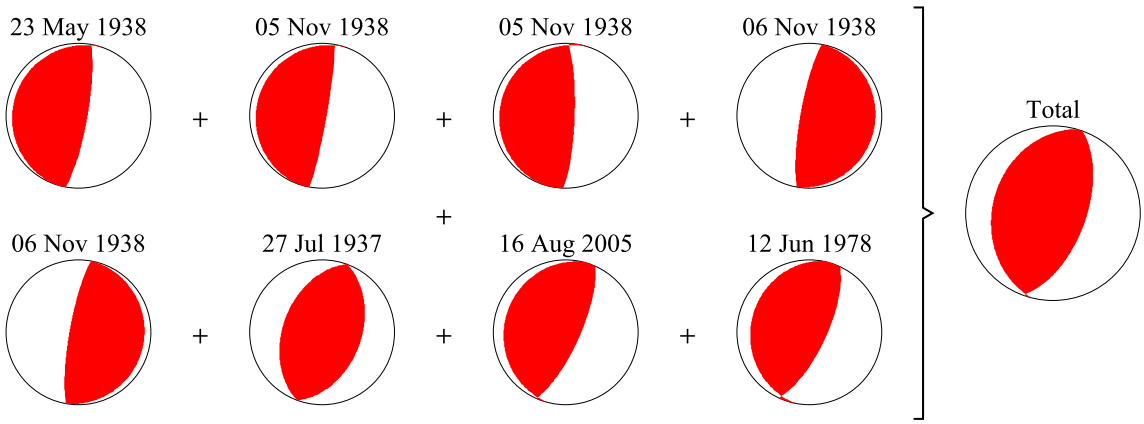

Figure 12. The Miyagi-oki sequence used to create the composite source along the Japan Trench. See Table S2 in Supporting Information S1 for details of focal mechanisms.

Umino et al., 2006), that is, roughly 50% of the 2011 mainshock rupture area. We replace the 1936 event with its colocated 2005 counterpart because of better data as shown in Figure 12 (also see Table S2 in Supporting Information S1). Using earthquake scaling laws (Geller, 1976) for a constant stress drop and assuming a uniform convergence rate along the trench, we first compute a field of static deformation for a source (model I) with the same seismic moment and mechanism as the 2011 Tohoku located at an average epicenter of the sequence (Figure 13Ia). We then design a second scenario (model II) as a source similar to model I, but with a smaller magnitude (M_w = 8.8) scaled down from the 2011 Tohoku mechanism (Figure 13IIa). As a third

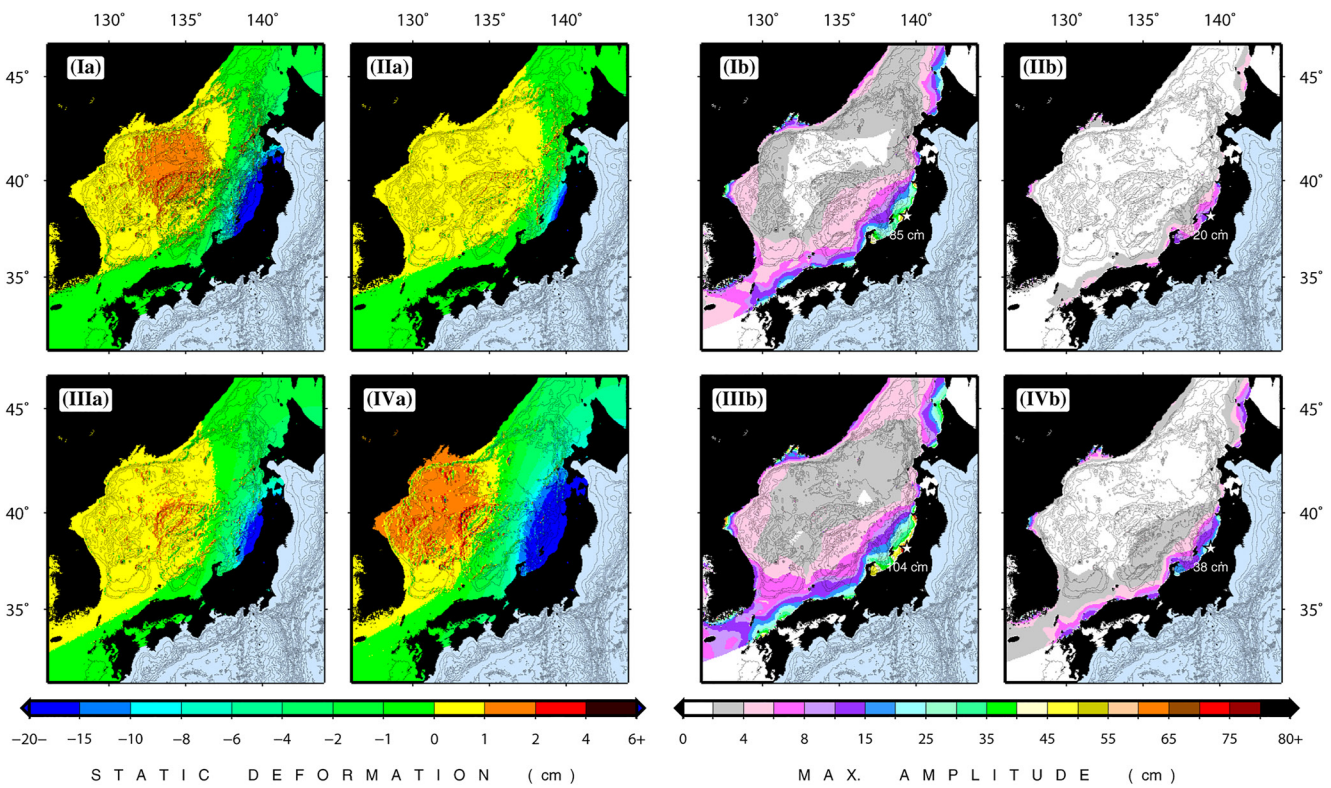

Figure 13. Sea floor deformation calculated for sources (Ia) identical to 2011 Tohoku but at the average epicenter of the 1936–1978 sequence, (IIa) with the same geometry as 2011 Tohoku at this location, but with smaller moment to match the smaller rupture area (M_w = 8.8), (IIIa) with a composite mechanism from the 1936–1978 sequence and a moment scaled down to rupture area, and (IVa) same as (IIIa) with a moment increased to that of the 2011 Tohoku. (Ib)-(IVb) Maximum tsunami amplitudes from simulation of (Ia) to (IVa) scenarios. The fore-arc area is masked to focus on the back-arc tsunami.

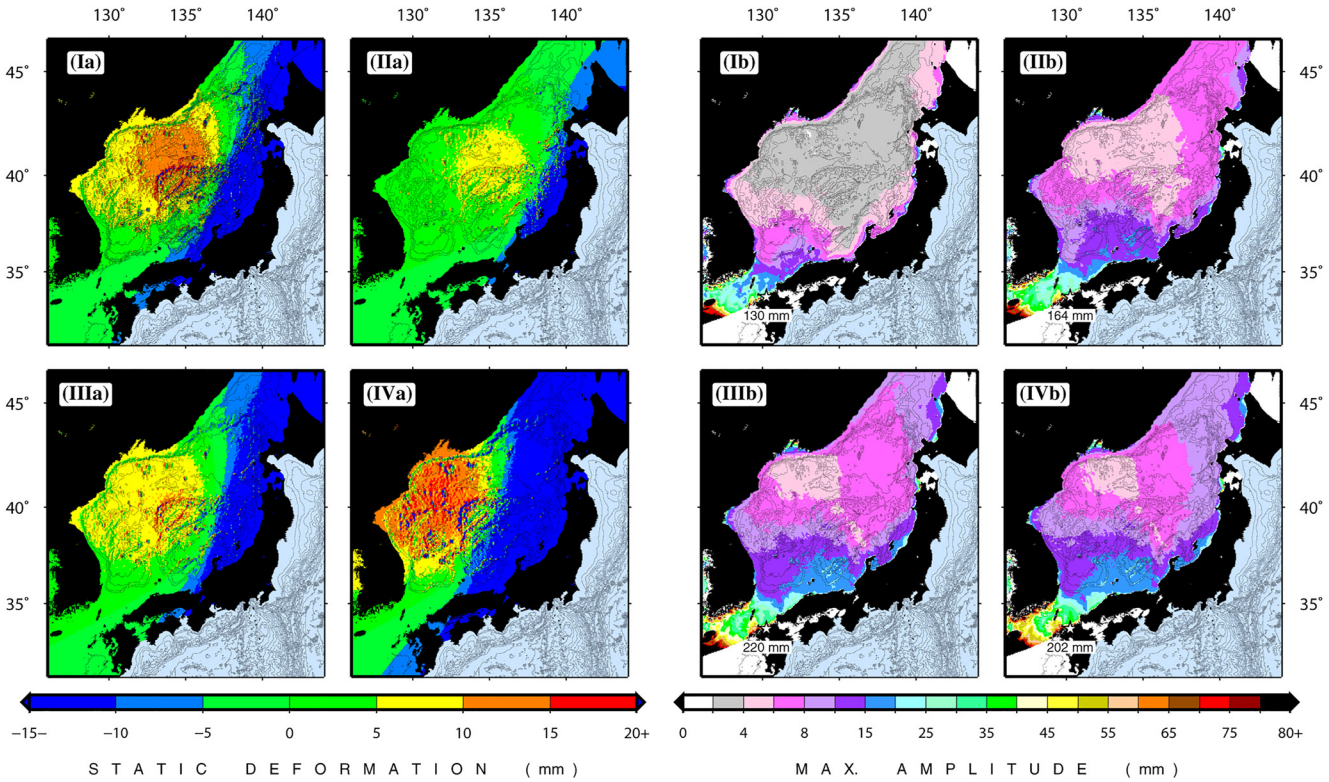

Figure 14. (Ia–IVa) Sea floor deformation fields from the four source scenarios in the Nankai Trough. (Ib–IVb) Fields of maximum amplitudes from the sources in (Ia–IVa).

scenario (model III), we make a composite mechanism by superimposing the 1936–1978 sequence and assigning a scaled down moment (M_w = 8.8) to match the rupture area (Figure 13IIIa). This mechanism has a Kagan aperture (Kagan, 1991) of ∼23° from the 2011 Tohoku. Lastly, we design a fourth scenario (model IV) with the same mechanism as model III, but with a moment equal to that of 2011 Tohoku. We then simulate the back-arc tsunamis from these sources using the same hydrodynamic conditions from Section 4.3. These simulations show that while the back-arc propagation patterns of the composite sources are fairly similar (CC = 0.55), the maximum tsunami amplitudes from the large source are twice as large as the smaller event. Also, back-arc tsunami amplitudes close to ∼1 m are expected near Niigata at the coast of Japan, similar to the 2011 event (see Figure 13).

5.2. Nankai Trough

While $M > 8$ earthquakes have been frequently documented in the Nankai Trough (Ishibashi, 2004), M∼9 events are also deemed possible through joining all the segments in single large ruptures (Yokota et al., 2016). Using the same simulation conditions as in Sections 4.1.3 and 5.1, we simulate back-arc tsunamis in the Sea of Japan for four rupture scenarios from combinations of the blocks proposed by Furumura et al. (2011) as shown in Figure 14Ia to 14IVa. Various permutations in the used blocks result in sources with M_w = 8.6 (model I) and M_w = 8.8 (models II to IV) (see Section S11 in Supporting Information S1 for more details). Simulation results for these scenarios are shown in Figures 14Ib and 14IVb (note the different color palettes used in Figures 13 and 14). These simulations suggest that earthquakes in the Nankai Trough would generate very small tsunamis in the Sea of Japan, barely reaching 10 cm. This is mainly due to a very wide (>400 km) continental arc and shallow continental shelf in the back-arc region. While the ruptures in these scenarios are closer to Busan compared to those in the Japan Trench (Section 5.1), the back-arc arrivals at Busan are negligible. This is probably due to the very shallow back-arc basin in the Korea Strait (<150 m deep) which results in significant attenuation. Similarly, the trapped edge waves on the shallow continental shelf from the fore-arc tsunami may not be notable at Busan due to their long paths in very shallow waters.

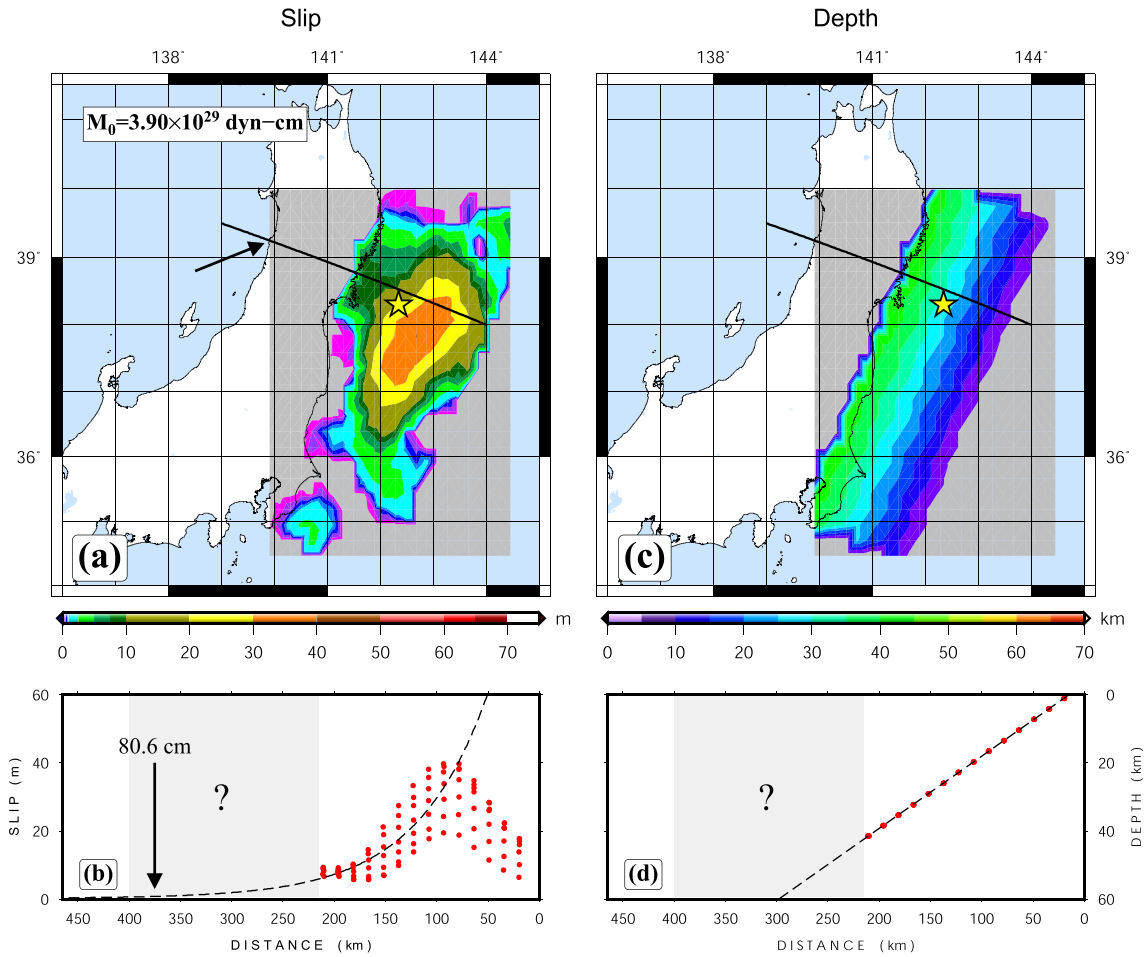

Figure 15. (a) Slip distribution of the 2011 Japan rupture from the finite fault solution by Ammon et al. (2011); yellow star shows the rupture centroid. (b) Cross section of the slip model along the solid black line in (a); the dashed curve is an exponential fit to the slip values. The solid arrow shows the location of western Japanese shoreline also marked in (a) and the extrapolated slip from the fit. (c) Depth model used in the model in (a). (d) Cross section of the depth model along the solid black line in (a and c); the dashed line is a linear fit to the depth values. The hatched areas in (c and d) denoted by question mark show the region not covered by the source model (data from SRCMOD; Mai & Thingbaijam, 2014).

6. Discussion and Conclusion

We present a simple dislocation model as the source of back-arc tsunamis explaining various features of these events (Figures 2 and 7). Our results show that the most important source parameter affecting back-arc tsunamis is seismic moment which controls rupture dimensions, especially the down-dip extent of dislocation. We find that among the geometrical source parameters, the energy of back-arc tsunamis is only affected by dip angle (δ in Figures 2 and 7). In this regard, our simulation of synthetic scenarios in flat oceans show that back-arc tsunami energetics (as a measure of tsunami frequency or wavenumber; e.g., Okal (2021)) are inversely proportional to dip of rupture plane. This is due to the effect of dip on the dominant frequency of back-arc tsunamis. We attribute this to the influence of dip angle on the surface expression of rupture, or the effective fault width. In our dipping plane model, a shallower dip of fault plane would result in a wider *area* of surface deformation (i.e., a larger length scale) and hence increasing the dominant period of the excited tsunami. Conversely, we report a rise in maximum back-arc tsunami amplitudes as a result of increasing dip angle for large megathrusts (Figure 6). This is due to the larger size of deformation at higher dip angle as expected from theory of elastic deformation.

Fault width can be routinely approximated from focal geometry and seismic moment using earthquake scaling laws. We note that, finite rupture models are often confined to the tectonic fore-arc regions (e.g., Figure 15 for the 2011 Tohoku-Oki earthquake), and the lower edge of the rupture remains somewhat speculative (see Section S1 in Supporting Information S1). This is due to the fact that the extent of back-arc deformation for megathrust ruptures

(the hatched areas in Figures 15b and 15d) is mainly possible by down-dip extrapolation of slip distribution. One must note that valid estimates of the down-dip extent of deformation are usually derived from physical models (e.g., Scholz, 1982). This lack of constraint in the back-arc prevents the use of finite fault models in studying back-arc tsunamis. While the mentioned extrapolation result may provide some insight regarding the order of magnitude of back-arc tsunamis in the near- and far-field, it does not lead to meaningful details about propagation and frequency content of the waveforms (see the block analysis in Section S12 in Supporting Information S1). We also note the importance of understanding the extent of back-arc deformation as it can lead to a more complete picture of the coseismic rupture (e.g., Shen et al., 2005). Such models provide valuable alternatives to the otherwise non-unique values obtained from various methods (e.g., as manifested in the various solutions for the 2011 Tohoku rupture in the SRCMOD database (Mai & Thingbaijam, 2014); also see Supporting Information S1).

We find that ruptures with larger dip angles create larger and more widespread tsunamis in the back-arc, as shown quantitively via the metric MT as well as in Figure 4. Thus, large megathrust earthquakes ($M_w \geq 9.0$) with intermediate dip angles (~20°) are expected to create larger, more hazardous tsunamis in back-arc basins. Based on this model, the effective width calculated as the extent of back-arc depression in a direction perpendicular to the trench determines the main properties of back-arc tsunamis (Figures 7 and 8). While larger ruptures result in slip fields closer to surface (i.e., producing more significant surface deformation), the focal depth of such events does not seem to have a significant impact (Figures 7–9).

Our simulations of back-arc tsunamis for the Sea of Japan form the 2011 Tohoku rupture confirm Murotani et al.'s (2015) conclusion on the significant contribution of horizontal deformation and the effect of complex bathymetry. In addition, we find that the contribution of Rayleigh waves to back-arc tsunami amplitudes, especially in the case of small static deformations, must be considered at regions with simple bathymetry (e.g., sites such as Rudnaya Pristan at the northwestern margin of the Sea of Japan). In locations at or near deformation nodes, addition of surface waves would potentially improve the quality of simulations, especially at higher (although low-amplitude) frequencies. This is best demonstrated in the case of Busan and Okushiri which were located at a deformation node of the 2011 Tohoku event.

Numerical simulations of the back-arc tsunamis from sources at and around the Japan Trench reveal the potential of back-arc tsunamis with coastal amplitudes reaching more than 1 m in western Japan and up to ~50 cm on the far side of the Sea of Japan (Figure 13). While such amplitudes are very small compared to the fore-arc run-up values (i.e., >20 m close to the epicenter) and often ignored in the wake of fore-arc catastrophes, they must be taken seriously in a basin which is otherwise deemed as safe from tsunamis. We emphasize that the reported coastal amplitudes from the simulations in this study are at a distance from the coastlines and are thus smaller than run-up (Synolakis, 1991). In other words, the on-land tsunami amplitudes will be relatively larger than our calculations while following similar along-coast patterns. As predicted by our dislocation model, our simulation of potential sources near Honshu with a larger dip angle compared to 2011 Tohoku leads to a larger back-arc tsunami (also see Section S10 in Supporting Information S1).

Simulation of tsunamis from potential sources in the Nankai Trough reveal that these ruptures will not create significant tsunami hazard (with amplitudes smaller than 10 cm) in the Sea of Japan. We attribute this deficiency in back-arc tsunami amplitudes (compared to the cases in Japan Trench) to the wider continental arc as well as a large, shallow continental shelf in the southern back-arc. Similar to the case of ruptures in Japan Trench, small coseismic amplitudes in Korea are due to the close proximity to deformation nodes.

While our simple model does not consider non-uniform slip which can result in uncertainties in resolving definitive rupture dimensions, we note that such deficiencies (e.g., in depth, dip angle, and seismic moment) are inherent to seismic, acoustic, and hydrodynamic analyses of the source (e.g., see Section 2.1). Also, some regions such as Java seem to be immune to the back-arc tsunami hazard due to the large trench-to-coast distance (an average of ~450 km) and thus will stand out as outliers in our model. Similarly, our model is not sufficient for small or very large ruptures, that is, M8 and $M \geq 9.5$ (although we note that the former is too small to excite notable back-arc tsunamis and the latter is extremely rare) and thus serves as first step in understanding back-arc tsunamis. It is important to note that the mismatch between predicted and simulated results is due to the under- and over-sampling of small (M8.5) and large (M9.5) sources.

Nevertheless, our model provides valuable constraints to the source in conjunction with other methods; the addition of any proxies on the down-dip extent of large megathrust ruptures is important in improving the otherwise

obscured aspect of source dimensions. Our model can be readily used for M9 events in subduction zones with back-arc basins around the world as our results show the possibility of relatively large tsunami amplitudes in the back-arc. Based on our results, tsunami hazard needs to be assessed and mitigated in various back-arc regions including Alaska-Aleutians, Peru-Chile, the Philippines, Sumatra (see Section S13 in Supporting Information S1) and Oaxaca in Mexico (e.g., Saloor et al., 2020). This issue is especially important in the back-arc of Oaxaca, that is, the Gulf of Mexico where highly populated regions and important economic facilities such as oil structures are exposed to high risk due to a very narrow continental arc (~200 km) and possibility of large megathrusts. While some limitations will arise from subduction zones with wider continental shelves and back-arc basins, our model can yet prove useful by making adjustments to initial seismic parameters (Saloor et al., 2020).

Conflict of Interest

The authors declare no conflicts of interest relevant to this study.

Data Availability Statement

The bathymetry data used in this study is publicly available via GEBCO (GEBCO, 2021). The tsunami simulation code is maintained and distributed by NOAA (https://nctr.pmel.noaa.gov/nthmp/). Tide gauge data is available at the Flanders Marine Institute (VLIZ) (2022) via the Intergovernmental Oceanographic Commission (IOC) Sea Level Station Monitoring Facility (http://www.ioc-sealevelmonitoring.org/map.php) and Geospatial Information Authority of Japan (GSI) (https://www.gsi.go.jp/kanshi/tide_furnish.html). The finite rupture data was acquired from SRCMOD (Mai & Thingbaijam, 2014) available at http://equake-rc.info/srcmod.

Acknowledgments
The authors are grateful to Satoko Murotani for sharing tide gauge data from the Japanese stations, and for providing accounts of the 2011 Tohoku back-arc tsunami. We also thank Emile Okal for discussions on synthesis of surface waves. The bathymetry data used in this study is publicly available via GEBCO (GEBCO, 2021). The tsunami simulation code is maintained and distributed by NOAA. Tide gauge data is available through the Sea Level Station Monitoring Facility (http://www.ioc-sealevelmonitoring.org/map.php) and Geospatial Information Authority of Japan (GSI) (https://www.gsi.go.jp/kanshi/tide_furnish.html). Several figures were created using Generic Mapping Tools (Wessel & Smith, 1998). This study was funded by National Science Foundation grant PREEVENTS geosciences directorate No. 1663769.

References

Abe, K. (1977). Tectonic implications of the large Shioya-Oki earthquakes of 1938. *Tectonophysics*, *41*(4), 269–289. https://doi.org/10.1016/0040-1951(77)90136-6

Abe, K. (2006). Dominant periods of the 2004 Sumatra tsunami and the estimated source size. *Earth Planets and Space*, *58*(2), 217–221. https://doi.org/10.1186/bf03353381

Ammon, C. J., Lay, T., Kanamori, H., & Cleveland, M. (2011). A rupture model of the 2011 off the Pacific coast of Tohoku Earthquake. *Earth Planets and Space*, *63*(7), 693–696. https://doi.org/10.5047/eps.2011.05.015

Ando, M. (1975). Source mechanisms and tectonic significance of historical earthquakes along the Nankai Trough, Japan. *Tectonophysics*, *27*(2), 119–140. https://doi.org/10.1016/0040-1951(75)90102-x

Aranguiz, R., Catalán, P. A., Cecioni, C., Bellotti, G., Henriquez, P., & González, J. (2019). Tsunami resonance and spatial pattern of natural oscillation modes with multiple resonators. *Journal of Geophysical Research: Oceans*, *124*(11), 7797–7816. https://doi.org/10.1029/2019jc015206

Barberopoulou, A., Qamar, A., Pratt, T. L., Creager, K. C., & Steele, W. P. (2004). Local amplification of seismic waves from the Denali earthquake and damaging seiches in lake union, Seattle, Washington. *Geophysical Research Letters*, *31*(5), L03607. https://doi.org/10.1029/2003gl018569

Berkhoff, J. C. W. (1976). Mathematical models for simple harmonic linear water waves: Wave diffraction and refraction (Vol. *123p*).

Bilek, S. L., & Lay, T. (2018). Subduction zone megathrust earthquakes. *Geosphere*, *14*(4), 1468–1500. https://doi.org/10.1130/ges01608.1

Chlieh, M., Avouac, J. P., Hjorleifsdottir, V., Song, T. R. A., Ji, C., Sieh, K., et al. (2007). Coseismic slip and afterslip of the great M_w 9.15 Sumatra–Andaman earthquake of 2004. *Bulletin of the Seismological Society of America*, *97*(1A), S152–S173. https://doi.org/10.1785/0120050631

Duputel, Z., Rivera, L., Fukahata, Y., & Kanamori, H. (2012). Uncertainty estimations for seismic source inversions. *Geophysical Journal International*, *190*(2), 1243–1256. https://doi.org/10.1111/j.1365-246x.2012.05554.x

Dziewonski, A. M., Chou, T. A., & Woodhouse, J. H. (1981). Determination of earthquake source parameters from waveform data for studies of global and regional seismicity. *Journal of Geophysical Research*, *86*(B4), 2825–2852. https://doi.org/10.1029/jb086ib04p02825

Ekström, G., Nettles, M., & Dziewonski, A. M. (2012). The global CMT project 2004–2010: Centroid-moment tensors for 13,017 earthquakes. *Physics of the Earth and Planetary Interiors*, *200*, 1–9. https://doi.org/10.1016/j.pepi.2012.04.002

Flanders Marine Institute (VLIZ). (2022). Intergovernmental Oceanographic Commission (IOC): Sea level station monitoring facility. https://doi.org/10.14284/482

Fujiwara, T., Kodaira, S., No, T., Kaiho, Y., Takahashi, N., & Kaneda, Y. (2011). The 2011 Tohoku-Oki earthquake: Displacement reaching the trench axis. *Science*, *334*(6060), 1240. https://doi.org/10.1126/science.1211554

Furumura, T., Imai, K., & Maeda, T. (2011). A revised tsunami source model for the 1707 Hoei earthquake and simulation of tsunami inundation of Ryujin Lake, Kyushu, Japan. *Journal of Geophysical Research: Solid Earth*, *116*(B2), 17. https://doi.org/10.1029/2010jb007918

GEBCO. (2021). *GEBCO Compilation Group*. GEBCO 2021 Grid. https://doi.org/10.5285/c6612cbe-50b3-0cff-e053-6c86abc09f8f

Geller, R. J. (1976). Scaling relations for earthquake source parameters and magnitudes. *Bulletin of the Seismological Society of America*, *66*(5), 1501–1523.

Gica, E., Teng, M. H., Liu, P. L. F., Titov, V., & Zhou, H. (2007). Sensitivity analysis of source parameters for earthquake-generated distant tsunamis. *Journal of Waterway, Port, Coastal, and Ocean Engineering*, *133*(6), 429–441. https://doi.org/10.1061/(asce)0733-950x(2007)133:6(429)

Grapenthin, R., & Freymueller, J. T. (2011). The dynamics of a seismic wave field: Animation and analysis of kinematic GPS data recorded during the 2011 Tohoku-Oki earthquake, Japan. *Geophysical Research Letters*, *38*(18), L18308. https://doi.org/10.1029/2011gl048405

Grue, J., Pelinovsky, E. N., Fructus, D., Talipova, T., & Kharif, C. (2008). Formation of undular bores and solitary waves in the Strait of Malacca caused by the 26 December 2004 Indian Ocean tsunami. *Journal of Geophysical Research*, *113*(C5), C05008. https://doi.org/10.1029/2007jc004343

Hartzell, S. H., & Heaton, T. H. (1983). Inversion of strong ground motion and teleseismic waveform data for the fault rupture history of the 1979 Imperial Valley, California, earthquake. *Bulletin of the Seismological Society of America*, *73*(6A), 1553–1583. https://doi.org/10.1785/bssa07306a1553

Hashimoto, C., Noda, A., Sagiya, T., & Matsu'ura, M. (2009). Interplate seismogenic zones along the Kuril–Japan trench inferred from GPS data inversion. *Nature Geoscience*, *2*(2), 141–144. https://doi.org/10.1038/ngeo421

Heidarzadeh, M., & Satake, K. (2013). Waveform and spectral analyses of the 2011 Japan tsunami records on tide gauge and DART stations across the Pacific Ocean. *Pure and Applied Geophysics*, *170*(6), 1275–1293. https://doi.org/10.1007/s00024-012-0558-5

Ide, S., Baltay, A., & Beroza, G. C. (2011). Shallow dynamic overshoot and energetic deep rupture in the 2011 Mw 9.0 Tohoku-Oki earthquake. *Science*, *332*(6036), 1426–1429. https://doi.org/10.1126/science.1207020

Ishibashi, K. (2004). Status of historical seismology in Japan. *Annals of Geophysics*, *47*(2–3), 338–369.

Ito, T., Ozawa, K., Watanabe, T., & Sagiya, T. (2011). Slip distribution of the 2011 off the Pacific coast of Tohoku earthquake inferred from geodetic data. *Earth Planets and Space*, *63*(7), 627–630. https://doi.org/10.5047/eps.2011.06.023

Ito, T. T., Osada, Y., Kido, M., Inazu, D., Hayashi, Y., Tsushima, H., et al. (2011). Frontal wedge deformation near the source region of the 2011 Tohoku-Oki earthquake. *Geophysical Research Letters*, *38*(7), L00G05. https://doi.org/10.1029/2011gl048355

Kagan, Y. Y. (1991). 3-D rotation of double-couple earthquake sources. *Geophysical Journal International*, *106*(3), 709–716. https://doi.org/10.1111/j.1365-246x.1991.tb06343.x

Kanamori, H., Rivera, L., & Lambotte, S. (2019). Evidence for a large strike-slip component during the 1960 Chilean earthquake. *Geophysical Journal International*, *218*(1), 1–32. https://doi.org/10.1093/gji/ggz113

Kido, M., Osada, Y., Fujimoto, H., Hino, R., & Ito, Y. (2011). Trench-normal variation in observed seafloor displacements associated with the 2011 Tohoku-Oki earthquake. *Geophysical Research Letters*, *38*(24), L24303. https://doi.org/10.1029/2011gl050057

Kim, S., Kang, T. S., Rhie, J., & Baag, S. Y. (2019). Validating slip distribution models of the 2011 Tohoku earthquake with diffracted tsunami and uplift-induced sea waves in the backarc region. *Geophysical Journal International*, *216*(3), 1578–1593. https://doi.org/10.1093/gji/ggy509

Kundu, P. K., Cohen, I. M., & Dowling, D. R. (2015). *Fluid mechanics* (p. 928p). Academic Press.

Lay, T. (2018). A review of the rupture characteristics of the 2011 Tohoku-oki Mw 9.1 earthquake. *Tectonophysics*, *733*, 4–36. https://doi.org/10.1016/j.tecto.2017.09.022

Lay, T., Ammon, C. J., Kanamori, H., Koper, K. D., Sufri, O., & Hutko, A. R. (2010). Teleseismic inversion for rupture process of the 27 February 2010 Chile (Mw 8.8) earthquake. *Geophysical Research Letters*, *37*(13), L13301. https://doi.org/10.1029/2010gl043379

Lay, T., Kanamori, H., Ammon, C. J., Nettles, M., Ward, S. N., Aster, R. C., et al. (2005). The great Sumatra-Andaman earthquake of 26 December 2004. *Science*, *308*(5725), 1127–1133. https://doi.org/10.1126/science.1112250

Lee, J. W., Park, E. H., Park, S. C., Lee, D. K., & Lee, J. H. (2016). Numerical simulations of the 2011 Tohoku, Japan tsunami forerunner observed in Korea using the bathymetry effect. *Journal of Korean Society of Coastal and Ocean Engineers*, *28*(5), 265–276. https://doi.org/10.9765/kscoe.2016.28.5.265

Mai, P. M., & Thingbaijam, K. K. S. (2014). SRCMOD: An online database of finite-fault rupture models. *Seismological Research Letters*, *85*(6), 1348–1357. https://doi.org/10.1785/0220140077

Mansinha, L. A., & Smylie, D. E. (1971). The displacement fields of inclined faults. *Bulletin of the Seismological Society of America*, *61*(5), 1433–1440. https://doi.org/10.1785/bssa0610051433

Meng, L., Inbal, A., & Ampuero, J. P. (2011). A window into the complexity of the dynamic rupture of the 2011 Mw 9 Tohoku-Oki earthquake. *Geophysical Research Letters*, *38*(7), L00G07. https://doi.org/10.1029/2011gl048118

Mori, N., Takahashi, T., Yasuda, T., & Yanagisawa, H. (2011). Survey of 2011 Tohoku earthquake tsunami inundation and run-up. *Geophysical Research Letters*, *38*(7), L00G14. https://doi.org/10.1029/2011gl049210

Murotani, S., Iwai, M., Satake, K., Shevchenko, G., & Loskutov, A. (2015). Tsunami forerunner of the 2011 Tohoku earthquake observed in the Sea of Japan. *Pure and Applied Geophysics*, *172*(3–4), 683–697. https://doi.org/10.1007/s00024-014-1006-5

Noda, H., & Lapusta, N. (2013). Stable creeping fault segments can become destructive as a result of dynamic weakening. *Nature*, *493*(7433), 518–521. https://doi.org/10.1038/nature11703

Okada, Y. (1985). Surface deformation due to shear and tensile faults in a half-space. *Bulletin of the Seismological Society of America*, *75*(4), 1135–1154. https://doi.org/10.1785/bssa0750041135

Okal, E. A. (2021). The energy of a tsunami generated by dynamic uplift of the ocean bottom. I. Analytical solutions. *Pure and Applied Geophysics*, *178*(12), 1–15. https://doi.org/10.1007/s00024-021-02804-0

Okal, E. A., & Synolakis, C. E. (2004). Source discriminants for near-field tsunamis. *Geophysical Journal International*, *158*(3), 899–912. https://doi.org/10.1111/j.1365-246x.2004.02347.x

Plafker, G. (1997). Catastrophic tsunami generated by submarine slides and backarc thrusting during the 1992 earthquake on eastern Flores I., Indonesia. *Geological society of America, cordilleran section*, *29*, 57. (abstract with programme).

Pollitz, F. F. (1996). Coseismic deformation from earthquake faulting on a layered spherical Earth. *Geophysical Journal International*, *125*(1), 1–14. https://doi.org/10.1111/j.1365-246x.1996.tb06530.x

Pollitz, F. F., Bürgmann, R., & Banerjee, P. (2011). Geodetic slip model of the 2011 M9.0 Tohoku earthquake. *Geophysical Research Letters*, *38*(7), L00G08. https://doi.org/10.1029/2011gl048632

Rabinovich, A. B. (1997). Spectral analysis of tsunami waves: Separation of source and topography effects. *Journal of Geophysical Research*, *102*(C6), 12663–12676. https://doi.org/10.1029/97jc00479

Saito, T., Baba, T., Inazu, D., Takemura, S., & Fukuyama, E. (2019). Synthesizing sea surface height change including seismic waves and tsunami using a dynamic rupture scenario of anticipated Nankai trough earthquakes. *Tectonophysics*, *769*, 228166. https://doi.org/10.1016/j.tecto.2019.228166

Salaree, A., Huang, Y., Ramos, M. D., & Stein, S. (2021). Relative tsunami hazard from segments of Cascadia subduction zone for Mw 7.5–9.2 earthquakes. *Geophysical Research Letters*, *48*(16), e2021GL094174. https://doi.org/10.1029/2021GL094174

Salaree, A., & Okal, E. A. (2015). Field survey and modelling of the Caspian sea tsunami of 1990 June 20. *Geophysical Journal International*, *201*(2), 621–639. https://doi.org/10.1093/gji/ggv044

Salaree, A., & Okal, E. A. (2020). Effects of bathymetry complexity on tsunami propagation: A spherical harmonics approach. *Geophysical Journal International*, *223*(1), 632–647. https://doi.org/10.1093/gji/ggaa334

Salditch, L., Stein, S., Neely, J., Spencer, B. D., Brooks, E. M., Agnon, A., & Liu, M. (2020). Earthquake supercycles and long-term fault memory. *Tectonophysics*, *774*, 228289. https://doi.org/10.1016/j.tecto.2019.228289

Saloor, N., Salaree, A., & Huang, Y. (2020). Back-arc tsunami hazard in the Gulf of Mexico from Oaxaca earthquakes: Lessons from past events. *AGU Fall Meeting Abstracts*, *2020*, NH017-07.

Satake, K. (2015). Geological and historical evidence of irregular recurrent earthquakes in Japan. *Philosophical Transactions of the Royal Society A: Mathematical, Physical & Engineering Sciences*, *373*(2053), 20140375. https://doi.org/10.1098/rsta.2014.0375

Satake, K., Ishibe, T., Murotani, S., Mulia, I. E., & Gusman, A. R. (2022). Effects of uncertainty in fault parameters on deterministic tsunami hazard assessment: Examples for active faults along the eastern margin of the Sea of Japan. *Earth Planets and Space*, *74*(1), 1–20. https://doi.org/10.1186/s40623-022-01594-6

Sato, M., Ishikawa, T., Ujihara, N., Yoshida, S., Fujita, M., Mochizuki, M., & Asada, A. (2011). Displacement above the hypocenter of the 2011 Tohoku-Oki earthquake. *Science*, *332*(6036), 1395. https://doi.org/10.1126/science.1207401

Scholz, C. H. (1982). Scaling laws for large earthquakes: Consequences for physical models. *Bulletin of the Seismological Society of America*, *72*(1), 1–14.

Shao, G., Li, X., Ji, C., & Maeda, T. (2011). Focal mechanism and slip history of the 2011 M w 9.1 off the Pacific coast of Tohoku Earthquake, constrained with teleseismic body and surface waves. *Earth Planets and Space*, *63*(7), 559–564. https://doi.org/10.5047/eps.2011.06.028

Shen, Z. K., Lü, J., Wang, M., & Bürgmann, R. (2005). Contemporary crustal deformation around the southeast borderland of the Tibetan Plateau. *Journal of Geophysical Research*, *110*(B11), B11409. https://doi.org/10.1029/2004jb003421

Shevchenko, G., Ivelskaya, T., & Loskutov, A. (2014). Characteristics of the 2011 great Tohoku tsunami on the Russian far East Coast: Deep-water and coastal observations. *Pure and Applied Geophysics*, *171*(12), 3329–3350. https://doi.org/10.1007/s00024-013-0727-1

Shimozono, T., Sato, S., Okayasu, A., Tajima, Y., Fritz, H. M., Liu, H., & Takagawa, T. (2012). Propagation and inundation characteristics of the 2011 Tohoku tsunami on the central Sanriku coast. *Coastal Engineering Journal*, *54*(01), 1250004. https://doi.org/10.1142/s0578563412500040

Stein, S., & Okal, E. A. (2011). The size of the 2011 Tohoku earthquake need not have been a surprise. *Eos, Transactions American Geophysical Union*, *92*(27), 227–228. https://doi.org/10.1029/2011eo270005

Synolakis, C. E. (1991). Green's law and the evolution of solitary waves. *Physics of Fluids A: Fluid Dynamics*, *3*(3), 490–491. https://doi.org/10.1063/1.858107

Synolakis, C. E., Bernard, E. N., Titov, V. V., Kânoğlu, U. T. K. U., & Gonzalez, F. I. (2008). Validation and verification of tsunami numerical models. In *Tsunami science four years after the 2004 indian ocean tsunami* (pp. 2197–2228).

Tang, L., Titov, V. V., & Chamberlin, C. D. (2009). Development, testing, and applications of site-specific tsunami inundation models for real-time forecasting. *Journal of Geophysical Research: Oceans*, *114*(C12), C12025. https://doi.org/10.1029/2009jc005476

Tanioka, Y., & Satake, K. (1996). Tsunami generation by horizontal displacement of ocean bottom. *Geophysical Research Letters*, *23*(8), 861–864. https://doi.org/10.1029/96gl00736

Thingbaijam, K. K. S., Martin Mai, P., & Goda, K. (2017). New empirical earthquake source-scaling laws. *Bulletin of the Seismological Society of America*, *107*(5), 2225–2246. https://doi.org/10.1785/0120170017

Titov, V., Kânoğlu, U., & Synolakis, C. (2016). Development of MOST for real-time tsunami forecasting. *Journal of Waterway, Port, Coastal, and Ocean Engineering*, *142*(6), 03116004. https://doi.org/10.1061/(asce)ww.1943-5460.0000357

Titov, V. V., & Gonzalez, F. I. (1997). Implementation and testing of the method of Splitting tsunami (MOST) model. *NOAA Technical Memorandum ERL PMEL-112*, 14p. Contribution No. 1927.

Titov, V. V., Mofjeld, H. O., González, F. I., & Newman, J. C. (1999). Offshore forecasting of Hawaiian tsunamis generated in Alaskan-Aleutian subduction zone. *NOAA Technical Memorandum ERL PMEL*, *114*, 22p.

Titov, V. V., & Synolakis, C. E. (1995). Modeling of breaking and nonbreaking long-wave evolution and runup using VTCS-2. *Journal of Waterway, Port, Coastal, and Ocean Engineering*, *121*(6), 308–316. https://doi.org/10.1061/(asce)0733-950x(1995)121:6(308)

Titov, V. V., & Synolakis, C. E. (1998). Numerical modeling of tidal wave runup. *Journal of Waterway, Port, Coastal, and Ocean Engineering*, *124*(4), 157–171. https://doi.org/10.1061/(asce)0733-950x(1998)124:4(157)

Umino, N., Kono, T., Okada, T., Nakajima, J., Matsuzawa, T., Uchida, N., et al. (2006). Revisiting the three M-7 Miyagi-oki earthquakes in the 1930s: Possible seismogenic slip on asperities that were re-ruptured during the 1978 M= 7.4 Miyagi-oki earthquake. *Earth Planets and Space*, *58*(12), 1587–1592. https://doi.org/10.1186/bf03352666

Ward, S. N. (1980). Relationships of tsunami generation and an earthquake source. *Journal of Physics of the Earth*, *28*(5), 441–474. https://doi.org/10.4294/jpe1952.28.441

Weatherall, P., Marks, K. M., Jakobsson, M., Schmitt, T., Tani, S., Arndt, J. E., et al. (2015). A new digital bathymetric model of the world's oceans. *Earth and Space Science*, *2*(8), 331–345. https://doi.org/10.1002/2015ea000107

Wessel, P., & Smith, W. H. (1998). New, improved version of generic mapping Tools released. *Eos, Transactions American Geophysical Union*, *79*(47), 579. https://doi.org/10.1029/98eo00426

Yanenko, N. N. (1971). *The method of fractional steps*. Springer.

Yokota, Y., Ishikawa, T., Watanabe, S. I., Tashiro, T., & Asada, A. (2016). Seafloor geodetic constraints on interplate coupling of the Nankai Trough megathrust zone. *Nature*, *534*(7607), 374–377. https://doi.org/10.1038/nature17632

References From the Supporting Information

Gilbert, F., & Dziewonski, A. M. (1975). An application of normal mode theory to the retrieval of structural parameters and source mechanisms from seismic spectra. *Philosophical Transactions of the Royal Society of London. in: Series A Mathematical and Physical Sciences*, *278*(1280), 187–269.

Kanamori, H., & Cipar, J. J. (1974). Focal process of the great Chilean earthquake May 22, 1960. *Physics of the Earth and Planetary Interiors*, *9*(2), 128–136. https://doi.org/10.1016/0031-9201(74)90029-6

Kanamori, H. (1970). Synthesis of the long-period surface waves and its application to earthquake source studies–Kurile Islands earthquake of October 13, 1963. *Journal of Geophysical Research*, *75*(26), 5011–5027. https://doi.org/10.1029/jb075i026p05011

Kian, R. (2015). *Tsunami induced wave and current amplification and sedimentation in closed basins*. (Doctoral dissertation, Ph. D. Dissertation) (p. 189). Middle East Technical University.

Koketsu, K., Yokota, Y., Nishimura, N., Yagi, Y., Miyazaki, S. I., Satake, K., et al. (2011). A unified source model for the 2011 Tohoku earthquake. *Earth and Planetary Science Letters*, *310*(3–4), 480–487. https://doi.org/10.1016/j.epsl.2011.09.009

Okal, E. A. (1976). A surface-wave investigation of the rupture mechanism of the Gobi-Altai (December 4, 1957) earthquake. *Physics of the Earth and Planetary Interiors*, *12*(4), 319–328. https://doi.org/10.1016/0031-9201(76)90027-3

Okal, E. A. (2017). The excitation of tsunamis by deep earthquakes. *Geophysical Journal International*, *209*(1), 234–249. https://doi.org/10.1093/gji/ggx013

Rost, S., & Thomas, C. (2002). Array seismology: Methods and applications. *Reviews of Geophysics*, *40*(3), 2–1. https://doi.org/10.1029/2000rg000100

Saito, M. (1967). Excitation of free oscillations and surface waves by a point source in a vertically heterogeneous Earth. *Journal of Geophysical Research*, *72*(14), 3689–3699. https://doi.org/10.1029/jz072i014p03689

Salaree, A., & Okal, E. A. (2020). Tsunami simulations along the Eastern African coast from mega-earthquake sources in the Indian Ocean. *Arabian Journal of Geosciences*, *13*(20), 1–13. https://doi.org/10.1007/s12517-020-05893-8

Satake, K. (1988). Effects of bathymetry on tsunami propagation: Application of ray tracing to tsunamis. *Pure and Applied Geophysics*, *126*(1), 27–36. https://doi.org/10.1007/bf00876912

Seno, T., Shimazaki, K., Somerville, P., Sudo, K., & Eguchi, T. (1980). Rupture process of the Miyagi-Oki, Japan, earthquake of June 12, 1978. *Physics of the Earth and Planetary Interiors*, *23*(1), 39–61. https://doi.org/10.1016/0031-9201(80)90081-3

Woods, M. T., & Okal, E. A. (1987). Effect of variable bathymetry on the amplitude of teleseismic tsunamis: A ray-tracing experiment. *Geophysical Research Letters*, *14*(7), 765–768. https://doi.org/10.1029/gl014i007p00765